LUND UNIVERSITY

FACULTY OF SCIENCE

Thermal neutron counting and gamma-ray peak identification from fusion reactions, using a Sodern Genie-16 Neutron Generator

Auden Ti Yun

Thesis submitted for the degree of Bachelor of Science, 15 hp
Project duration: 2 months

Supervisor: Robert Frost
Co-supervisor: Nicholai Mauritzson, Kevin Fissum, Mikael Elfman

Department of Physics
Division of Nuclear Physics
Autumn Semester 2021

Abstract

This thesis work focuses on the categorisation of a Sodern Genie-16 Neutron Generator, at the Nuclear Applications Laboratory, Lund University. To that end, the goals of this work focuses on the re-development of the pre-existing infrastructure surrounding the Sodern Genie-16 Neutron Generator for the purposes of internally irradiating samples, and the subsequent categorisation of the new configuration for extraction of fast neutrons. The purpose of this is to expand the potential applications, such as for neutron time-of-flight studies. To fully take advantage of the re-development, the neutron cave housing the Sodern Genie-16 Neutron Generator needs to also retain the ability to internally irradiate samples. The reconfiguration of the neutron cave was achieved by placing the neutron box containing the Sodern Genie-16 Neutron Generator atop a turntable assembly, where the fast neutrons are guided with a collimated exit port out of the neutron cave. Next, to categorise the new configuration, two separate sets of measurements were taken: thermal-neutron counting was performed using a ^{3}He proportional counter on 15 positions corresponding to a grid; and γ-ray measurements were achieved using a HPGe detector at one fixed position of the grid. The analysis of the thermal-neutron counting measurements yielded a fitting function that provides a reasonable prediction of the thermal-neutron count rate in the laboratory space. The analysis of the background and background-corrected γ-ray spectrum yielded identification of γ-rays from thermal-neutron capture reactions, and fast-neutron induced reactions. Two potential γ-rays candidates from DT fusion from the Sodern Genie-16 Neutron Generator were also identified, which might serve the purpose of neutron time-of-flight studies.

Contents

List of Figures

List of Abbreviations

ANP	Applied Nuclear Physics
CANS	Compact Accelerator-driven Neutron Source
CoMPASS	CAEN Multi-Parameter Spectroscopy Software
DAQ	Data Acquisition
DD	Deuterium-Deuterium
DT	Deuterium-Tritium
ENDF	Evaluated Nuclear Data File
ENSDF	Evaluated Nuclear Structure Data File
ESS	European Spallation Source
fe	First Escape
FWHM	Full Width at Half Maximum
G-16 NG	Sodern Genie 16 Neutron Generator
HPGe	High-Purity Germanium
HV	High Voltage
IAEA	International Atomic Energy Agency
MCA	Multi-Channel Analyser
NAA	Neutron Activation Analysis
NIST	National Institute of Standards and Technology
NNDC	National Nuclear Data Center
NuDat 3.0	Nuclear Structure and Decay Data 3.0
PC	Proportional Counter
PGAA	Prompt Gamma-ray Neutron Activation Analysis
se	Second Escape
SF6	Sulfur Hexafluoride
TOF	Time-Of-Flight

1 Introduction

Protons, neutrons, and electrons come together to form the atom, which is the building block for the universe. The atomic nucleus is composed of only protons and neutrons; the number of protons determine the element, while the number of neutrons determine the isotope of that element. A neutron has no charge and only a weak magnetic moment, and interacts primarily by the strong- and weak-nuclear forces. Free neutrons can be sourced in many different ways, such as natural radioactive decay, or artificially through nuclear reactions. The kinetic energy that a free neutron possesses changes the form of its interaction with matter. These different interactions can include elastic-scattering, inelastic-scattering and neutron-capture reactions. Elastic-scattering, primarily performed with low neutron energies, is useful for determining the structure, magnetic properties, and other physical properties of materials. Inelastic-scattering can result in the emission of radiations, such as γ-rays, from target materials. Neutron-capture reactions change the isotope of the capturing nucleus, which if unstable will decay to a different element.

This scientific thesis focuses on the categorisation of the Sodern Genie-16 Neutron Generator (G-16 NG), at the Nuclear Applications Laboratory, Lund University. The G-16 NG is a device for creating free neutrons through nuclear fusion reactions. These neutrons interact strongly with their environment, and therefore detailed measurements are required to separate between radiations emitted from the G-16 NG, and radiations emitted from neutron interactions with the local environment.

1.1 Background

Applied nuclear physics is one of the main research areas at the Division of Nuclear Physics, Lund University. The Applied Nuclear Physics (ANP) group, working in the Nuclear Applications Laboratory, has a strong history of ion-beam analysis [1, 2], environmental monitoring of radioactive nuclides [3], and applied neutron physics [4]. The Nuclear Applications Laboratory utilises a number of sources of free neutrons for: calibration and development of advanced detectors for neutron-scattering instrumentation [5]; development of instrumentation for the characterisation of spent nuclear fuel [6]; Neutron Activation Analysis (NAA) [7]; work on thermal-neutron tagging [8]; as well as educational purposes. In addition to radioisotope sources and a Compact Accelerator-driven Neutron Source (CANS), that is currently under construction, the sources of free neutrons used at the Nuclear Applications Laboratory include a G-16 NG. The G-16 NG produces fast-neutrons, with a near-isotropic distribution and peak yield at a kinetic energy of $\sim$14 MeV. The G-16 NG is factory calibrated to produce up to 5×10^8 n/s, depending on the voltage applied to the linear acceleration of the deuteron ion. The neutron production is $\sim$100 times higher than radioisotope sources, and $\sim$100 times lower than the CANS will be, making it an appropriate mid-level neutron source. The G-16 NG is housed within a 'neutron cave' constructed of efficient neutron shielding materials such as water and borated polyethylene, to provide radiation protection to users.

1.2 Project Goals and Motivations

The goals of this project focus on the re-development of the pre-existing infrastructure surrounding the G-16 NG, and the subsequent categorisation of this new configuration. These goals can be defined explicitly as:

1. reconfiguration of neutron cave for extraction of fast neutrons, while retaining its existing capability to internally irradiate samples;
2. measurement of thermal neutrons outside of the neutron cave, at a number of pre-defined positions;
3. measurement of γ-rays outside of the neutron cave, at a fixed position;
4. and identification of γ-rays from fusion reactions from a G-16 NG.

The neutron cave, with the G-16 NG, was originally built for the purpose of providing neutrons to experiments inside the cave. It is now desirable to expand the potential applications, such as neutron time-of-flight (TOF) studies, by enabling the extraction of fast neutrons. The need to retain the ability to internally irradiate samples in the neutron cave is to allow for the continued development of an NAA station, which once established, will be applied to purposes such as the environmental monitoring around the European Spallation Source (ESS). To take full advantage of the reconfigured set-up, as complete a categorisation as possible needs to be performed. When the G-16 NG is operational, thermal neutrons will scatter out from the neutron cave, affecting experiments performed outside. It is therefore important to categorise the thermal-neutron background, thus motivating project goal 2. Similarly, γ-rays emitted from neutron activation of the environment will affect experiments outside the neutron cave. The measurement of γ-rays therefore needs to be performed in a fixed position, at which an experimental set-up would most likely be placed, as per project goal 3. The motivation for project goal 4 is that identifying γ-rays from the fusion reactions in the G-16 NG is of particular interest, as these can potentially serve as the trigger for neutron TOF studies. Accomplishing the four project goals listed will benefit all current and future research work that requires the use of the G-16 NG.

1.3 Report Structure

Following this introduction, Chapter 2 outlines the theoretical background relevant to the project, covering the fundamentals of nuclear structure, neutrons and γ-rays. Next, Chapter 3 covers the experimental set-up at the Nuclear Applications Laboratory, thermal neutron measurements, and γ-ray measurements. In Chapter 4, the results of the thermal neutron and γ-ray measurements will be presented and discussed. Finally, Chapter 5 summarises the project, and gives recommendation for future work.

2 Theory

This chapter provides the theoretical background relevant to the experimental work performed, and the discussion of the results obtained. The nuclear structure of the atom is first discussed, followed by the production, interaction, and detection of γ-rays. Similarly, the production, interaction, and detection of free neutrons are covered. As the subject matter on these topics is extensive, only a cursory overview of each can be given here, and recommendations for further reading are therefore provided.

2.1 Nuclear Structure

2.1.1 Protons, Neutrons and Isotopes

In an atom, the nucleus is made up of nucleons: protons [9] and neutrons [10] held together by the strong nuclear force acting between them. The protons are positively charged, and the neutrons are uncharged. Protons and neutrons are also fermions, and therefore obey the Pauli exclusion principle, which states that no two identical fermions can occupy the same quantum state [11]. The number of protons and neutrons, and energy state define the nucleus of any atom. Any nuclide can be presented in the notation ${}^{\mathrm{A}}_{\mathrm{Z}}\mathrm{X}_{\mathrm{N}}$, where X is the chemical symbol of an element, Z is the number of protons, N is the number of neutrons, and A=(Z+N) is the mass number. The many different nuclei resulting from the possible combinations of Z and N can be presented on a chart of nuclides [12], and the number of protons determine the element of the nuclide, while the number of neutrons determine the isotope of the element. Isotopes are nuclides of the same element with the same number of protons, and differ only in the number of neutrons.

2.1.2 The Atomic Nucleus

The liquid drop model [13, 14, 15] describes the nucleus as a charged liquid-droplet. The nucleus is bound together by the binding energy (E_B), which can be approximated by the semi-empirical mass formula [16]:

$$E_B = a_{\mathrm{v}}A - a_{\mathrm{s}}A^{2/3} - a_{\mathrm{c}}\frac{Z^2}{A^{1/3}} - a_{\mathrm{sym}}\frac{(2Z-A)^2}{A} \pm a_{\mathrm{p}}\frac{((-1)^Z + (-1)^{(A-Z)})}{2A^{1/2}} \tag{2.1}$$

where the lower-case a and respective subscripts represent coefficients obtained by fitting the formula to experimental data. There are five terms contributing to the binding energy: the volume term, surface term, Coulomb term, asymmetry term, and pairing term. Detailed discussions of these terms can be found elsewhere [16, 17].

Nuclides with a mass number around 60 possess the highest E_B/nucleon, and are therefore the most stable. To reach the peak of binding energy, lighter nuclei can undergo nuclear fusion (see Section 2.1.4) to become heavier, while very heavy (A>200) nuclei can undergo

nuclear fission to become lighter. In either processes, the resultant nuclide may be unstable, and therefore decays with the emission of particle(s), to become stable. The types of decay that can bring a nucleus closer to stability are α-decay, β^--decay, β^+-decay, electron-capture and nucleon (proton or neutron) emission. More information on these different types of decay can be found elsewhere [18, 19, 20]. γ-ray emission and internal conversion are special types of radioactive decay that involves a change in energy state of the nucleus, defined by the organisation of its nucleons. Additional detail on γ-ray emission is presented in Section 2.1.3.

2.1.3 Excited and Metastable States

The nuclear shell model can provide complementary information to the liquid drop model. It is based on a quantum mechanical approach, in which the Pauli exclusion principle and fermion properties of the nucleons are built upon, allowing for nuclear structure to be defined as a quantum system with a number of energy states. The energy state of a nucleus can be described by the total nuclear angular momentum **J**, and parity π. For a nucleus to transition from a higher energy state to a lower energy state (de-excitation), a γ-ray of the energy difference between the two states is emitted. The lowest possible, and also most stable, energy state is the ground state, while an excited state is any energy state higher than the ground state. For a nucleus in an excited state to transition into its ground state, two extreme scenarios may occur: a single γ-ray with energy of the difference between the excited and ground state is emitted; or a γ-ray is emitted from the initial excited state to the next excited, albeit lower energy state. A γ-ray cascade occurs where γ-rays are emitted in a 'step-wise' de-excitation, until the nucleus reaches its ground state.

Following a decay that changes the Z and/or N of a nucleus, the product nucleus is usually created in an excited state, and therefore one or more γ-rays are emitted for the product nucleus to reach its ground state. The emission of a γ-ray is usually prompt ($<10^{-9}$ s), but there are long-lived excited states, called *metastable* states or isomers, that emit a γ-ray after an extended period of time, the most extreme case being $>10^{16}$ s [21]. In general, an unstable nucleus may decay only in its ground state, therefore metastable states may cause a 'γ-delayed' decay. In other words, an unstable nucleus in a metastable state is effectively blocked from decaying until a γ-ray is emitted. Further reading is available [20, 22, 23].

2.1.4 Nuclear Fusion

As briefly mentioned in Section 2.1.2, light nuclei fuse together to form a heavier nucleus in order to reach the peak of binding energy. Fusion between two light nuclei, such as two ^{2}H atoms, are possible, but so are two, considerably heavier atoms. Fusion reactions can be achieved through natural means (e.g. the Sun with proton-proton chain), or artificially, such as accelerating one nuclei against another. The latter process will be discussed in Section 2.3.2.

The fusion reaction between two light nuclei, deuterium-tritium (DT) and

deuterium-deuterium (DD), are described below:

$$\textbf{DT:} \quad {}^{2}\mathrm{H} + {}^{3}\mathrm{H} \longrightarrow {}^{4}\mathrm{He} + {}^{1}\mathrm{n} \qquad \text{Q-value} = +17.6 \text{ MeV} \tag{2.2}$$

$$\quad {}^{2}\mathrm{H} + {}^{3}\mathrm{H} \longrightarrow {}^{5}\mathrm{He} + \gamma \qquad \text{Q-value} = +16.9 \text{ MeV} \tag{2.3}$$

$$\textbf{DD:} \quad {}^{2}\mathrm{H} + {}^{2}\mathrm{H} \longrightarrow {}^{3}\mathrm{He} + {}^{1}\mathrm{n} \qquad \text{Q-value} = +3.26 \text{ MeV} \tag{2.4}$$

For DT fusion, two reactions are listed, where their branching ratio ${}^{3}\mathrm{H(d,\gamma)}/{}^{3}\mathrm{H(d,n)}$ is $(5.6 \pm 0.6) \times 10^{-5}$ [24]. The energy liberated from the ${}^{3}\mathrm{H(d,n)}{}^{4}\mathrm{He}$ reaction is shared between the two reaction products: $E_n = 14.1$ MeV and $E_\alpha = 3.2$ MeV. For the ${}^{3}\mathrm{H(d,\gamma)}$ reaction, the reaction product ${}^{5}\mathrm{He}$ is produced in an excited state, before de-excitation via γ-ray emission. Further reading of nuclear fusion reactions is available on [25, 26].

2.2 Gamma-rays

2.2.1 Gamma-ray Interaction with Matter

γ-rays, the production of which is described in Section 2.1.3 are electromagnetic radiation produced by nuclei. The energy of a γ-ray can be described as E=hν, with Planck's constant h, and frequency ν. γ-rays have no charge, and can interact with the electrons and nuclei. The major interaction mechanisms are:

$$\gamma + \text{target atom} \longrightarrow \begin{cases} \text{Photoelectric effect} \\ \text{Compton scattering} \\ \text{Pair production} \end{cases} \tag{2.5}$$

The type of interaction mainly depends on the energy of the incident γ-ray. At energies ($\sim$ keV) close to the binding energy of an electron in one of the bound shells of an atom, an incident γ-ray may be fully absorbed by the bound electron, resulting in the ejection of the now free, photoelectron. At higher energies, the γ-ray *Compton scatters* against a bound electron, that is, the incoming γ-ray partially transfers its energy to an electron at an angle. The "scattered" γ-ray then travels until it interacts with another atom. Pair production is possible at energies higher than 1.022 MeV, twice the rest mass of an electron (0.511 MeV). The incident γ-ray interacts with the nucleus of a target atom, and is transformed into an electron-positron pair of equal energy to the incident γ-ray. If the positron interacts with an electron (electron-positron annihilation), two γ-rays of 0.511 MeV are emitted in opposite directions.

A beam of γ-rays is attenuated by the forementioned interactions as it passes through matter. The intensity of the attenuated beam is given by:

$$I(x) = I_0 e^{(-\mu x)}, \tag{2.6}$$

where I_0 is the incident intensity, μ is the total absorption coefficient, and x is the thickness of the absorber. The total absorption coefficient of any absorber material is determined by the total cross section of each form of γ-ray interaction. Detailed discussion of γ-ray interaction, and attenuation can be found in [26, 27].

2.2.2 Gamma-ray Detection

There are many different types of γ-ray detectors, such as ionisation chambers, Geiger-counters, scintillation detectors, and semiconductor detectors. Semiconductor detectors utilises solid semiconductor materials such as silicon or germanium, that when ionised by interaction with γ-rays, result in a detection signal. In crystalline materials, electrons are confined to the valence band, and are separated by a bandgap to the the conduction band, where electrons are free to conduct electricity. Semiconductor materials have a small bandgap in between their conduction band and valence band, making it possible for an valence electron to gain energy to leave a hole (vacancy) at the valence band, and drift through to the conduction band. The production of these electron-hole pairs are increased when the crystal is ionised by a γ-ray, and the number of these electron-hole pairs correspond to the incident energy of the γ-ray.

A subset of these detectors are high-purity germanium (HPGe) detectors, which use Germanium crystals as the semiconducting material. These detectors provide good energy resolution of about 0.15%, but must be operated at temperatures of liquid nitrogen (-196 °C). pulse-height spectra obtained from the HPGe detector feature escape peaks and Compton edges. As presented in Section 2.2.1, if the incident γ-ray energy is larger than 1.02 MeV, two annihilation γ-rays of 0.511 MeV are emitted. The first escape (fe) peak is observed at 0.511 MeV below the incident γ-ray energy, while the second escape (se) peak is observed at 1.022 MeV below the incident γ-ray energy. The escape peaks are due to one or both of the annihilation γ-rays escaping the detector. The Compton edge corresponds to the maximum energy an electron gains ($E_{\max}$) when ionised by a incident γ-ray, and can be calculated with

$$E_{\max} = \frac{2E_\gamma^2}{2E_\gamma + m_e}, \tag{2.7}$$

where E_γ is the energy of the incident γ-ray, and m_e is the mass of a free electron. More information on γ-ray detection, HPGe detectors, and the features of γ-ray spectra are available elsewhere [28, 29, 30].

2.3 Neutrons

2.3.1 Neutron Interactions with Matter

Free neutrons interact with the target nucleus via scattering and absorption reactions, unlike charged particles that interact primarily via Coulomb forces. Possible neutron interactions are [31]:

$$\text{Scattering} \longrightarrow \begin{cases} \text{Elastic: (n,n)} \\ \text{Inelastic: (n,n')} \end{cases} \qquad \text{Absorption} \longrightarrow \begin{cases} \text{Electromagnetic: (n,}\gamma\text{)} \\ \text{Charged: (n,p), (n,}\alpha\text{), etc.} \\ \text{Neutral: (n,2n), (n,3n), etc.} \\ \text{Fission: (n,f)} \end{cases} \tag{2.8}$$

Conventionally, free neutron energies are categorised based on the cadmium cutoff of about 0.5 eV, *i.e.* the energy of abrupt drop in absorption cross section, into the "slow neutron" and "fast neutron" regions [26]. Of importance for neutron detection is the probability per

unit length for any interaction at any fixed energy, expressed as the cross section σ per nucleus, in units of *barn* (1 b = 10^{-28} m^2).

The slow neutron region has significant interactions of elastic scattering with target nuclei, and neutron-induced nuclear reactions. Due to the low kinetic energies of the neutrons, the neutron transfers little energy to the target nuclei during elastic scattering. However, this interaction is *very* probable, and serves as a basis for neutron moderation, and therefore most slow neutrons are moderated to an average energy of 0.025 eV, which are sub-categorised into *thermal neutrons*. Neutron-induced nuclear reactions, such as thermal-neutron capture, result in reaction products that can be measured. NAA is a nuclear process that relies on neutron capture reactions, to measure the γ-rays emitted from the compound and daughter nuclei. For fast neutrons, the cross section of any reaction mechanism occurring is very low. The most important interaction is the elastic scattering of fast neutrons, where the neutron transfers some of its kinetic energy to the scattering nucleus. Further discussion is found in [32].

2.3.2 Neutron Production

Free neutrons are produced naturally from spontaneous fission of transuranic radioisotopes, but can also be produced artificially from radioisotope (α,n) sources, radioisotope (γ,n) sources, nuclear reactions from accelerated charged particles, and from nuclear fission reactors.

Radioisotope (α,n) sources involve combining an α-emitting radioisotope and a target nuclide to emit free neutrons. A typical neutron source combination is the ^{241}Am/^{9}Be, where ^{241}Am α-decays into the products ^{237}Np, α-particle, and γ-ray. The α-particle then reacts with ^{9}Be to produce the excited compound nucleus ^{13}C*, which can decay via several modes, all of which emit a free neutron. Neutron generators, CANS, and spallation sources utilise nuclear reactions from accelerated charged particles to produce free neutrons. In-depth discussions of each neutron source is available at [20, 33, 34].

Neutron generators specifically use accelerated charged particles to produce neutrons with

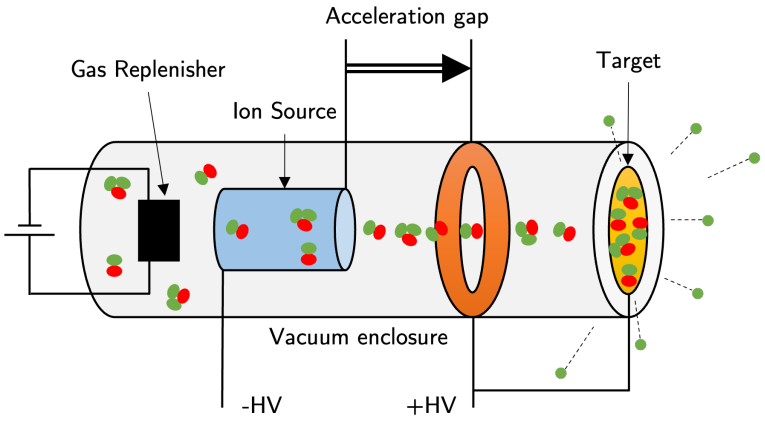

Figure 2.1: Schematic diagram of a neutron generator. The red oval represents a proton, while the green oval represents a neutron. The red and green oval pairs is deuterium, while the set of 2 green and 1 red ovals is tritium. The green circles represent free neutrons from the fusion reactions.

nuclear fusion reactions, as discussed in Section 2.1.4. A typical neutron generator consists primarily of an ion source, accelerator, and target. The Penning, or cold cathode, ion source is based on the Penning trap, and functions to ionise the deuterium gas to deuterons [35, 36]. The ions are then linearly accelerated by a potential of 100-300 kV, where they hit a metal hydride target containing tritium. Among the current neutron generator designs, the compact Penning diode neutron generator combines the ion source and diode structure for acceleration, and together with the target, is sealed in a tube. Further reading of neutron generator design and development is available at [35, 36].

2.3.3 Neutron Detection

Most techniques of neutron detection are performed indirectly. In general, information of incoming neutrons are inferred from the detection of secondary radiation from neutron absorption interactions. There are various types of neutron detectors available: Proportional counters (PC), TOF spectrometers, scintillation detectors, and semiconductor detectors.

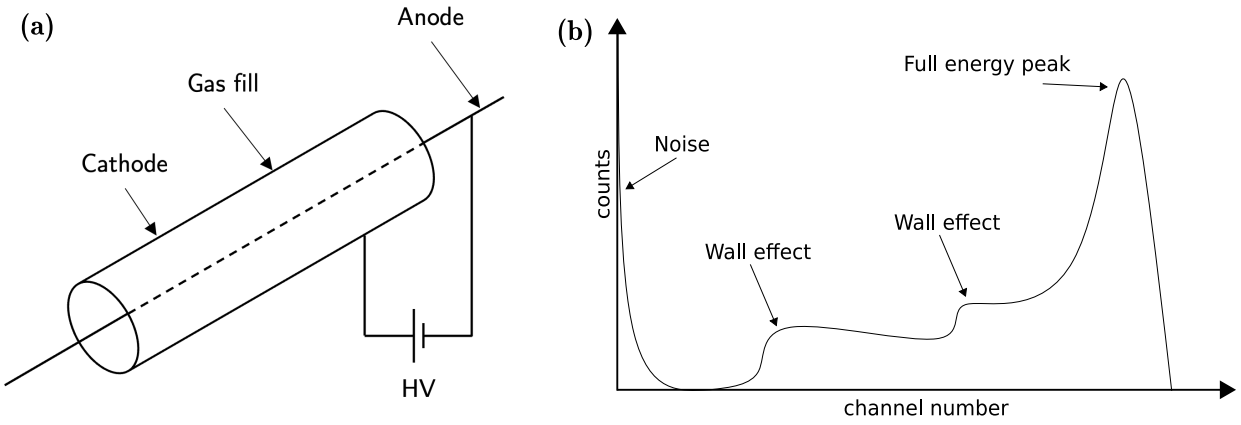

Figure 2.2: (a) Schematic diagram of a general cylindrical gas-filled PC. Adapted from [37]. (b) Expected pulse-height spectrum from a ^{3}He PC. The wall effect and full-energy peak features are shown.

The PC is a type of gas-filled detector, and relies on the phenomenon of gas multiplication to amplify detection signals. Figure 2.2(a) shows the schematic diagram of a general cylindrical PC. An incoming free neutron would react with the gas atoms in the PC, emitting reaction products that ionise the gas atoms, producing electron-ion pairs. The free electrons are accelerated by the electrical field created by the potential difference between the anode and cathode, and may collide with gas atoms while drifting to the anode, eventually creating a cascading phenomenon called a Townsend avalanche [38].

The noble gas ^{3}He is a widely used gas-fill for a PC, due to its high thermal-neutron cross section of 5330 barns. The neutron capture reaction with a free neutron is

$$^{3}\mathrm{He} + {}^{1}\mathrm{n} \longrightarrow {}^{3}\mathrm{H} + {}^{1}\mathrm{p} \qquad \text{Q-value} = 0.764 \text{ MeV}, \tag{2.9}$$

which produces the reaction product of a triton and a proton. Figure 2.2(b) presents the expected pulse-height spectrum with the wall effect and full-energy peak features. The kinetic energy of each reaction product is shared from the Q-value (in this case, energy released from the reaction), and if both reaction products deposit all their energy in the PC,

the full-energy peak is observed. The wall effects are due to one of the reaction products escaping from the PC without depositing its energy, and the plateau between the features are due to the reaction products partially depositing its energy before escaping the PC. The ^{3}He PC is used as a thermal neutron counter, where only the number of free neutrons that have interacted with the detector is measured. The detector is generally not used to measure fast neutrons due to the low cross section ($\sim 10^{0}$ barns) of the neutron-capture reaction. Further reading on neutron detectors, and ^{3}He PC is available at [30, 39, 40, 41].

3 Experiment

This chapter describes the experimental set-up at the Microbeam Hall. The operational parameters of the G-16 NG housed within the neutron cave, is first detailed. The layout of the neutron cave, and improvements made to the neutron box within the cave, is then discussed. Finally, a description of the two different measurement campaigns is presented: using a ^{3}He PC for thermal neutron measurements, and a HPGe detector for γ-ray measurements.

3.1 Neutron Generator and Neutron Cave

3.1.1 Neutron Generator

A photograph of the G-16 NG is shown in Figure 3.1. The G-16 NG is a vacuum-sealed tube (neutron tube) and consists of the following main components:

- Gas replenisher: To maintain gas mixture pressure inside tube
- Ion source: To ionise the gas mixture
- Ion accelerator: Polarised to very high voltage to accelerate gas ions
- Target: Accelerated ions hit the deuterium/tritium target, producing fast neutrons

Section 2.3.3 details the general operating principle of a neutron generator. The gas replenisher pressurises the gas mixture composing of deuterium and tritium to $\sim$0.1 Pa in the neutron tube [35], with pressure regulated through a replenisher resistor. Regulation of the gas pressure allows for the control and stabilisation of the eventual neutron emission. The gas mixture is then ionised under a maximum voltage of 2.5 kV, resulting in positively charged deuterons and tritons. The ions is then accelerated (polarised at voltages of -50 to -120 kV) toward the deuterium/tritium target, producing fast neutrons through the nuclear

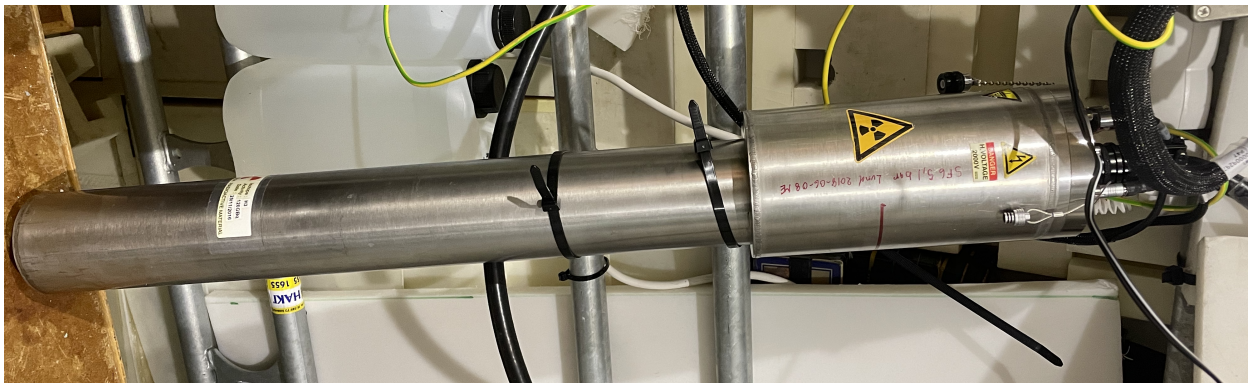

Figure 3.1: Photograph of the G-16 NG removed from the neutron box and bucket housing.

fusion reactions described in Section 2.3.2. Sulfur Hexafluoride (SF6) gas at 4-5 bars [42] surrounds the neutron tube, providing electrical insulation and thermal stability.

The G-16 NG is advertised [42] to produce fast neutron energies of 14 MeV (DT) and 2.5 MeV (DD), with yields of up to 4×10^8 n/s/4π sr and 4×10^6 n/s/4π sr, respectively. Neutron emission from the G-16 NG can be set in continuous or pulsed mode, but in the present work, only continuous mode is used. A stable continuous neutron emission of 4.7×10^8 n/s was reached before measurements are performed.

3.1.2 Neutron Cave

The G-16 NG was housed inside a plastic bucket filled with distilled water, separated by a 5 mm layer of clear plastic. The plastic bucket was housed in a box made of sheets of borated polyethylene, each sheet being 21 mm thick. A hole, 200 mm in diameter was made in the plastic bucket, acting as an exit port for fast neutrons. Schematic diagrams of the box and bucket is shown in Figure 3.2. The box was improved from previous neutron activation analysis work [7], with additional layers of borated polyethylene on the sides of the box, and a corresponding hole for the exit port. Additional layers of borated polyethylene, and pure polyethylene, are fitted into any empty space between the box and bucket for additional neutron shielding.

The box and bucket was contained within a 'neutron cave' that is structurally supported by steel beams and lumber. Figure 3.3 details the floor plan of the laboratory space in which the neutron cave was situated, and the detector placement grid. The neutron cave was situated in the corner, with two sides against concrete walls. The neutron cave was lined with walls of water containers, sheets of borated polyethylene, and blocks of wax in order to provide neutron shielding by moderating the fast neutrons generated from the G-16 NG. The approximate location of the neutron source in the G-16 NG is shown as a fuchsia rectangle, and the red areas show the wax collimator. The exit port is guided outside the neutron cave by a plastic pipe, where the detector placement grid is positioned. Two polyethylene-lined doors provided access into the neutron cave, and are connected to a kill-switch that cuts power to the G-16 NG when the doors are open. In addition, when the doors are closed and the G-16 NG is operational, a red lamp above the doors light up for visual cue on radiation safety measures.

The G-16 NG was used to produce a beam of collimated fast neutrons, as well as for NAA. To facilitate this dual purpose, the box and bucket was placed atop a turntable assembly, allowing the box and bucket to be rotated. To achieve a beam of collimated fast neutrons, the exit port was fitted with a wax collimator, and orientated to face the wall of the neutron cave which has a corresponding hole. To ensure proper alignment, a plastic pipe was inserted from outside the neutron cave that ends at the window of the bucket, providing a collimated beam. This orientation is shown in Figure 3.3. The box and bucket can also be orientated (about 90°) to face the pneumatic setup of the NAA system, where samples can be sent to the exit port.

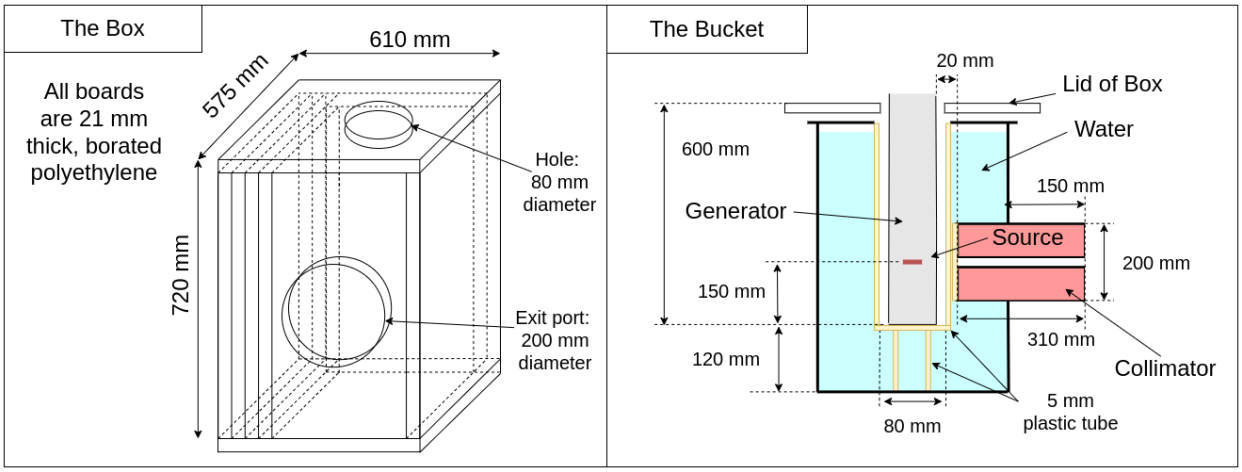

Figure 3.2: Schematic diagram of the G-16 NG bucket and box.

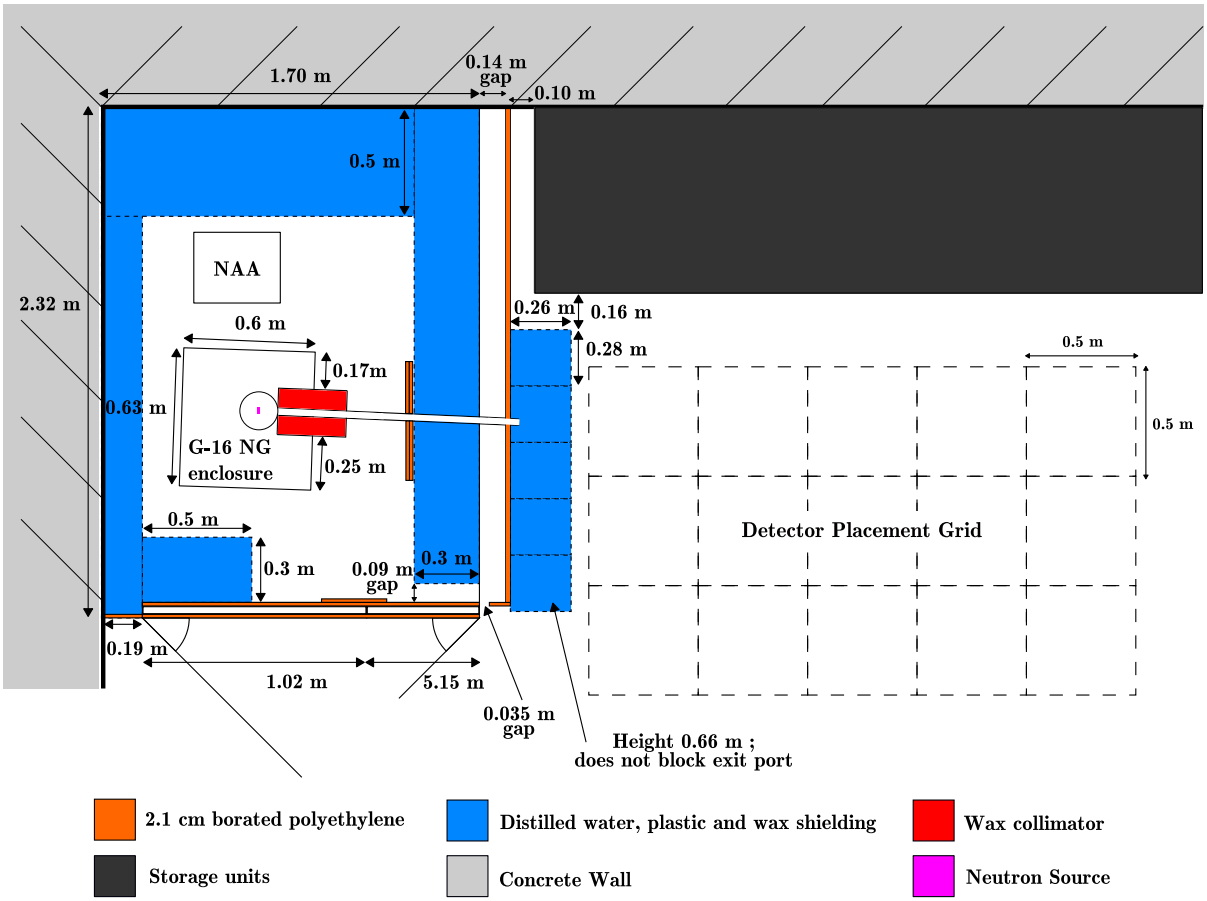

Figure 3.3: Floor plan of the laboratory space containing the neutron cave. The G-16 NG enclosure was orientated to produce collimated fast neutrons, directed at the first row of the detector placement grid.

3.2 Thermal Neutron Measurement

3.2.1 Detector Set-Up

The ^{3}He PC used for neutron detection was pressurised to 10 bars of ^{3}He gas, and was already efficiency calibrated, with $\varepsilon_{ff} = (96.1 \pm 0.3)$ % @ 2.5Å (neutron kinetic energy of 0.013 eV). The PC therefore has a high efficiency to detect cold and thermal ($\sim$ 0.025 eV) neutrons. Figure 3.4 shows the detector fitted in a stand for stability, and was connected to an ORTEC 142PC Preamplifier (pre-amp). The detector was run at High Voltage (HV) bias of +1500 kV, where the HV was connected to the pre-amp. The output signal from the detector was passed through a Canberra Model 2020 Spectroscopy Amplifier (spec-amp), with coarse gain of 10, fine gain of 4,70, and signal shaping time of 5 µs. The output from the spec-amp was run through the multi-channel analyser (MCA), ORTEC Easy-MCA, providing 8192 channels. The data acquisition (DAQ) software used was MAESTRO version 6.08.

3.2.2 Measurement Procedure

The ^{3}He neutron detector was set-up on a 3×5 grid outside the neutron cave, illustrated in Figure 3.3. The position **M0N0** was chosen as the origin **O** position, which had 3.7 m source-to-detector distance, and direct line-of-sight from the exit port. Each grid was 0.5 m × 0.5 m, with the detector at the centre of each grid. The columns of the grids are labelled **N0, N1, N2, N3** and **N4**. The rows are labelled **M0, M1** and **M2**. It should be noted that an Am/Be neutron source was stored 3.2 m from the **M2N4** position. For each grid position, a background measurement was taken for an average of ∼2000 seconds, with the exception of the origin position, which ran for about 4700 seconds. When the G-16 NG was turned on, measurements were taken at each grid position for average ∼2000 seconds. One additional measurement was performed at position **M2N4** with the Am/Be neutron source removed, and the G-16 NG turned off. The results are discussed in Section 4.1.

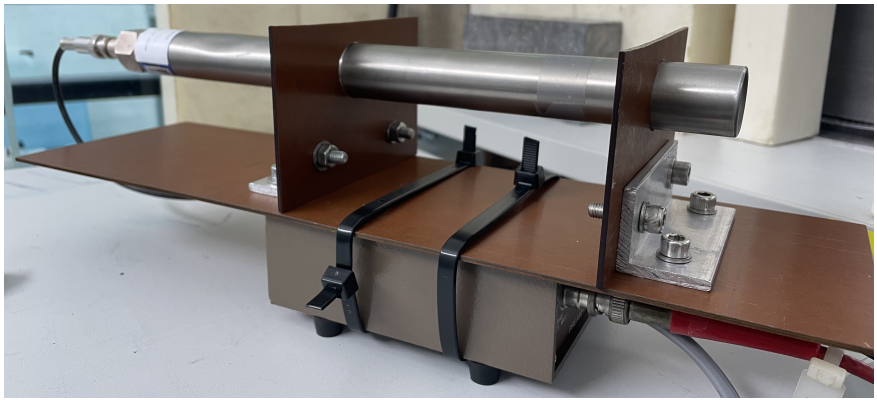

Figure 3.4: ^{3}He PC fitted in stand. The detector was connected to an ORTEC pre-amp attached under the stand.

3.3 Gamma-ray Measurement

3.3.1 Detector Set-Up

The HPGe detector used, seen in Figure 3.5(a), was a Canberra assembly of: Detector model GC2018, cryostat model 7935SL-2, and pre-amp model 2002CSL. The cryostat equipped to cool down the Germanium cylinder in the detector was filled with liquid nitrogen (-196 °C), and took about 4 hours (from room temperature) to be cooled-down and operational. The detector was run at positive HV bias of +3500 kV. The HPGe detector was connected to a CAEN Digital MCA (Model: DT5780P) which supports 16384 channels. The DAQ software used to obtain the pulse-height spectra is CAEN Multi-PArameter Spectroscopy Software (CoMPASS). Signal processing parameters were set in CoMPASS, as follows: Coarse gain: 1x, fine gain: 1, DC offset: 3 %, trapezoid rise time: 3.0 µs, and trapezoid flat top: 1.0 µs. The HPGe detector was placed at the origin **O** position of the detector placement grid. A total of $\sim$ 42 hours of background measurement was taken, and a total of $\sim$ 23 hours of measurement with the G-16 NG turned on.

3.3.2 Calibration of HPGe

A ^{152}Eu source of activity ~15 kBq was used to calibrate the HPGe detector. The source features well-known and intense γ-ray lines, of which 14 with the highest relative intensity were identified from the Evaluated Nuclear Data File (ENDF)/B-VIII.0 data library [44], and subsequently Gaussian-fitted to obtain the centroids of each peak in the spectrum. Using these data, a linear calibration was performed, that resulted in a bin width of $1.335 \pm 5.56 \times 10^{-4}$ keV, with an offset of 0.686 ± 0.171 keV.

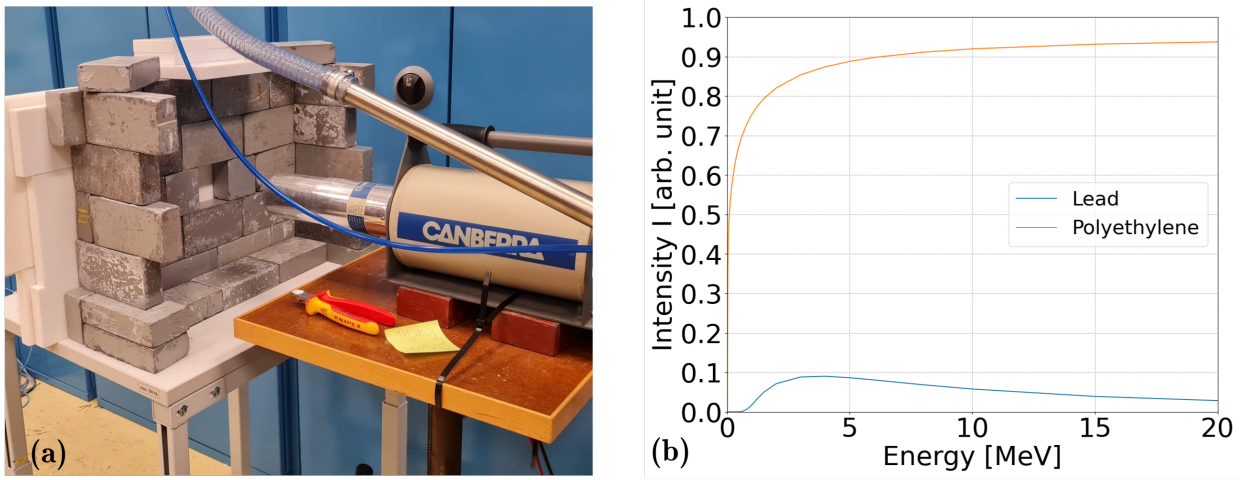

Figure 3.5: (a) HPGe detector set up 3.7 m away from the G-16 NG with direct line-of-sight. The lead and polyethylene shielding in front of the detector was meant to lower the count rates when the G-16 NG was turned on. (b) γ-ray intensity as a function of incoming γ-ray energy with the attenuation coefficients of lead and polyethylene obtained from National Institute of Standards and Technology (NIST) [43].

3.3.3 Dead Time Reduction

On initial measurement runs, when the G-16 NG was on, the detector experienced a dead-time of 4.08 %. This affected the efficacy of background-correction of the pulse-height spectrum, especially for energies above 10 MeV, as the count rates for energies around 20 MeV with the G-16 NG on was lower than the background count rates. A major contribution to the count rate at energies below 10 MeV was the fast-neutron activation of the germanium crystal in the detector, with a total cross section of $\sim$ 3.3 b for neutrons at 14 MeV. Another contribution was from the neutron activation of the external walls of the neutron cave and the surrounding laboratory space. As γ-rays from the fusion reaction were expected to fall in the higher energy range (see Section 2.1.4), it was necessary to address this problem.

To account for the count rate discrepancies when the G-16 NG was on, a wall of polyethylene 4.2 cm thick and lead 5.1 cm thick shielding was built to attenuate incoming free neutrons and γ-rays from the G-16 NG. The construction can be seen in Figure 3.5(a). The configuration was set-up 15 cm from the detector. γ-ray attenuation is discussed in Section 2.2.1 and the effects for the experimental set-up, obtained using Equation 2.6, are shown in Figure 3.5(b). The lead wall attenuated γ-rays by $\sim$90% for the energy range relevant to the experiment, which effectively reduced the overall count rate. An 8 x 8 cm hole in the lead wall, in line with the exit port, allowed energetic γ-rays from the G-16 NG to still be detected by the detector. The polyethylene wall served two purposes: reduction of germanium γ-rays from fast-neutron activation of the germanium, and attenuation of low energy γ-rays. The application of the wall shielding resulted in a reduced dead time of 1.24 %, hence improving the background-correction efficacy. The negative background-corrected count rates was no longer observed.

4 Results and Discussion

This chapter first presents the results obtained from the thermal neutron measurements, and discussions on the pulse-height spectra, heat-map of the neutron count rate, and the correspondence to the inverse-square law. Next, the γ-ray measurements presents background and background-corrected γ-ray spectra, and discusses the identified background γ-rays, neutron activated γ-rays, and γ-rays from the G-16 NG.

4.1 Thermal Neutron Measurement

4.1.1 Pulse-height Spectra from the ^{3}He PC

Figure 4.1 shows the background-corrected pulse-height spectrum measured at position **O** by the ^{3}He PC. Common to the spectra at all grid positions, the two wall effects, and full energy peak of the ^{3}He(n,p) neutron capture reaction can be seen. The spectrum features are discussed in Section 2.3.3. It should also be noted that the ^{3}He detector has relatively low sensitivity for detecting fast neutrons, by a factor of 2.29×10^{-5} relative to thermal-neutron, due to a much lower cross section. Events recorded were therefore assumed to be purely from thermal neutrons. By integrating over the region between the red vertical lines in Figure 4.1 (i.e. between the first wall effect and the full energy peak) of each background-corrected spectra, the thermal-neutron count rate was obtained. The count rates obtained for each position are presented as the heat map, featured in Figure 4.2.

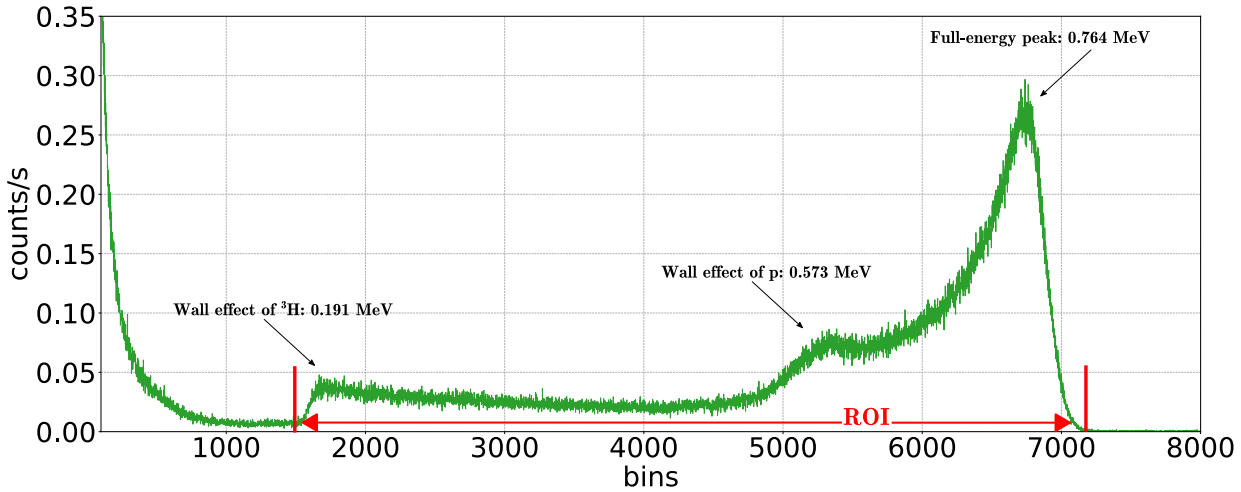

Figure 4.1: Background-corrected pulse-height spectrum at position **O**. The region of integration used to obtain thermal neutron count rate is marked between two vertical red lines.

4.1.2 Measurement Grid Outside the Neutron Cave

Figure 4.2 shows the floor plan of the neutron cave and experimental set-up, expanded from that shown in Figure 3.3, to also include the storage location of the Am/Be source. The detector placement grid is now overlaid with a heat map that shows the background-corrected thermal-neutron count rates for each position of the ^{3}He detector. At the bottom right of each grid position, a smaller square indicates the corresponding background thermal-neutron count rates. Both the background-corrected and background count rates have been corrected for detector-efficiency. It should be noted that the detector-efficiency was assumed for all slow neutrons, and was zero for fast neutrons, as the detector was calibrated for efficiency at one neutron energy, as mentioned in Section 3.2.1.

If the assumption is made that the collimator and neutron shielding of the neutron cave is ideal, and that only thermal and fast neutrons are emitted from the neutron cave via the exit port as a perfectly collimated beam, one would then expect that the thermal-neutron count rate to be constant at positions with direct line-of-sight to the exit port. This assumption is invalid for a number of reasons: that the neutron source from the G-16 NG is isotropic, the presence of neutron scattering effects inside the collimator, and that the neutron shielding is not ideal. This is supported by examining the measured thermal-neutron count rates in each of the columns of the detector placement grid. The highest thermal-neutron count was at column **N4**, which had the shortest source-to-detector distance, and the thermal-neutron count rate decreases with increasing distance. Furthermore, the highest thermal-neutron count rate was not at position **M0N4**, in front of the exit port, but at position **M2N4**. As is illustrated in Figure 4.2, there was a gap in the shielding (at the bottom right of the neutron cave as displayed in the figure), which allowed neutrons to escape. Coincidentally, position **M2N4** also has the highest background thermal-neutron count rate as it was the closest measurement position to the Am/Be neutron source.

4.1.3 Validation of Measurements Using Am/Be Background

The Am/Be neutron source was used to verify the heat map of the grid with the background thermal-neutron count rate. The neutron source was assumed as a point source, hence the inverse-square law correspondence was expected. The thermal-neutron count rate at each grid position was fitted with the point-source function:

$$y = \frac{a}{4\pi r^2} + c, \tag{4.1}$$

where a is the strength of the neutron source, r is the source-to-detector distance, and c is the background thermal-neutron count rate not attributed to the Am/Be source. A plot containing these data and the fitted function is shown in Figure 4.3. The uncertainty of each point was calculated using $\sqrt{N_t}/t_l$, where N_t is the integrated total counts in the ROI, and t_l is the live-time of the detector. From the fitted function, a was found to be 710±44 n/s, and c was found to be 5.45±0.21 n/s. To determine the goodness of fit of the fitted function, the reduced chi-square was calculated to be 83, which indicated slight underfitting.

The strength of the Am/Be neutron source was $\sim 10^6$ n/s, however, as the neutron source was contained inside a shielded barrel, the actual strength of the Am/Be neutron source *outside* the shielded barrel is unknown. The fitted value of a is not unreasonable, but without knowledge of the actual strength of the Am/Be neutron source, ultimately cannot be validated. The additional background measurement performed at position **M2N4** with the

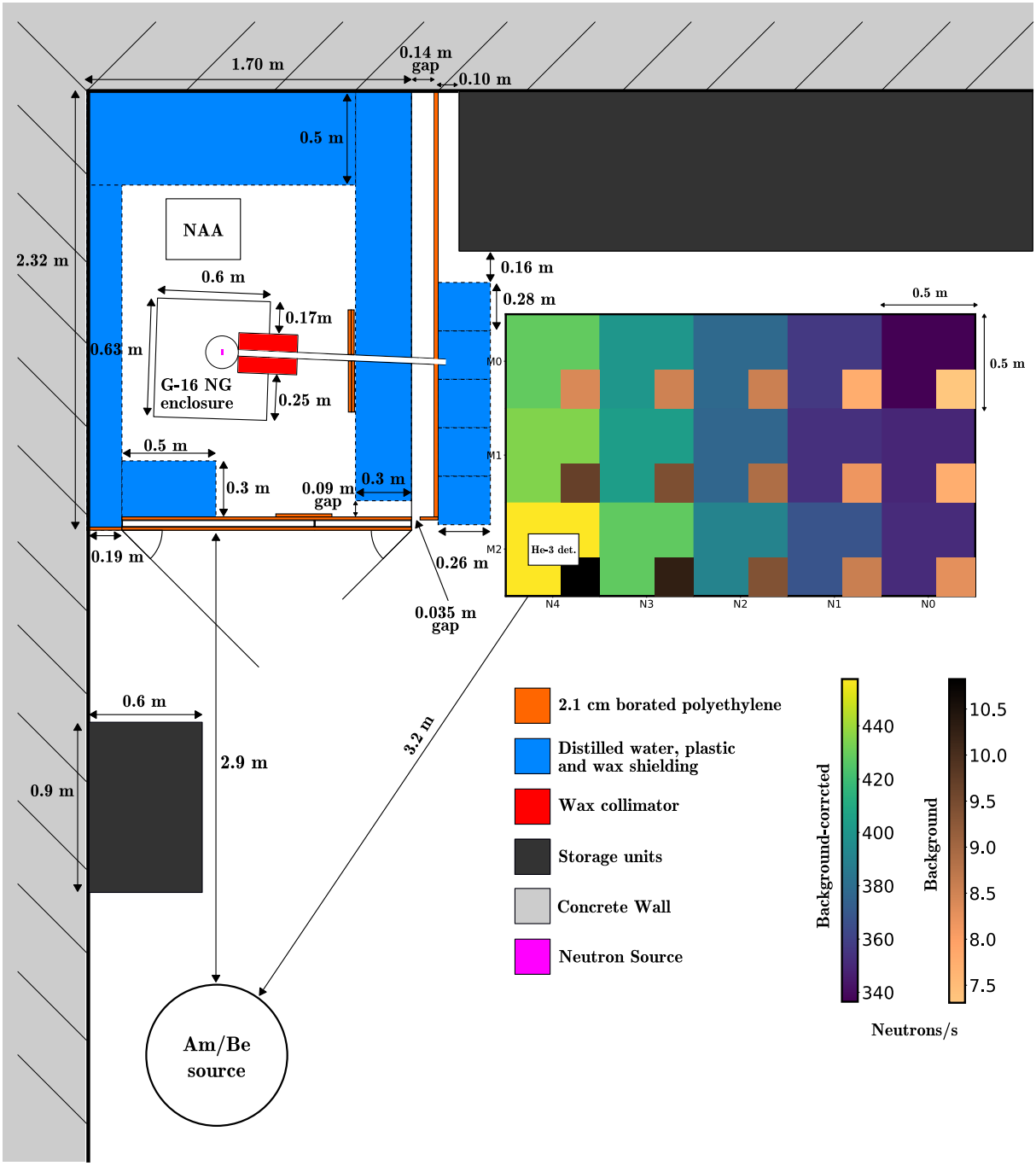

Figure 4.2: Extended floor plan of the neutron cave including the relevant distances to the Am/Be source. The background-corrected heat map is placed over the detector placement grid featured in Figure 3.3. The inset within each grid position of the heat map shows the background count rate.

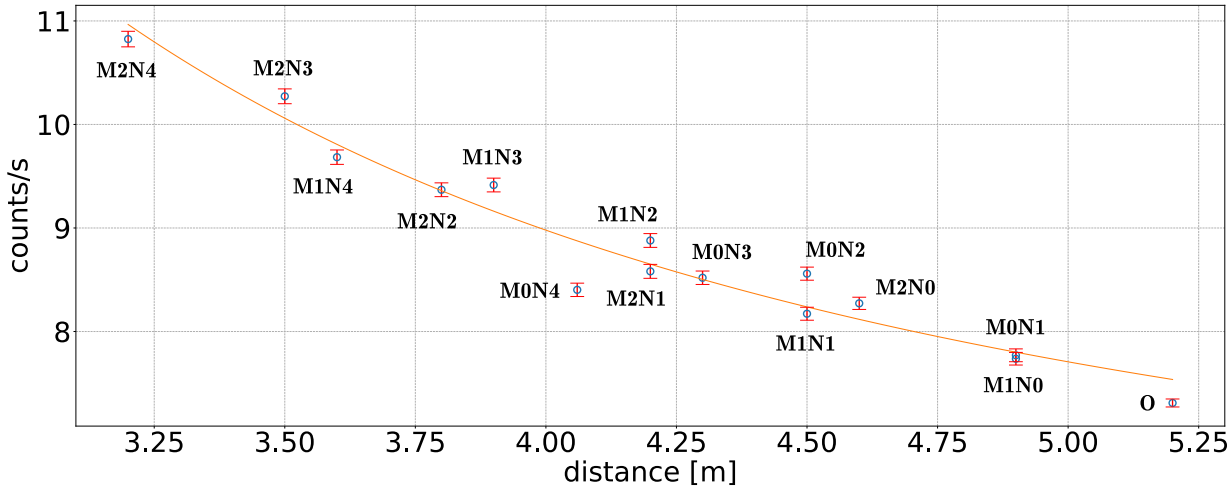

Figure 4.3: Thermal-neutron count rate as a function of distance from the Am/Be neutron source, using all positions on the grid. The points are hollow blue circles, with associated error bars in red. The point-source function fit is represented by the orange line.

Am/Be neutron source removed yielded a thermal-neutron count rate of 0.8±0.02 n/s. This count rate represents the thermal-neutron background at the laboratory space not attributed to the Am/Be source, and is one order of magnitude lower than the fitted value of c. The discrepancies between the count rates and fitted function are due to two main factors: the experimental set-up is not in free space, and the Am/Be neutron source contained inside a barrel is not a point source. As the laboratory space is not in free space, neutrons are scattered against the concrete walls, floor, and objects within the space. In addition, the Am/Be neutron source contained inside the shielded barrel, with dimensions 37 cm in diameter and 48 cm in height, that cannot be treated as a point source. Considering these factors, the point source assumption function produces a surprisingly reasonable fit.

4.1.4 Thermal Neutron Measurement in Line-of-Sight of the G-16 NG

The same inverse-square law validation was also performed with the first row **M0** of the heat map. The background-corrected thermal neutron count rates, with detector-efficiency correction, were used. The uncertainty at each point was obtained in the same manner as per the background thermal-neutron count rates. In addition to fitting with Equation 4.1, an additional linear-source fit was performed using:

$$y = \frac{a}{2\pi r} + c. \tag{4.2}$$

From Equation 4.1, the variables were found to be $a = 3993 \pm 622$ n/s and $c = 325 \pm 10$ n/s, and the percentage uncertainty was found to be 9.3% for variable a. From Equation 4.2, the variables were found to be $a = 1772 \pm 164$ n/s and $c = 267 \pm 11$ n/s, with percentage uncertainty of 15.6% for variable a. The reduced chi-square values were 579 and 211, for the point-source fit, and linear-source fit, respectively. The large values of both reduced chi-square indicated poor fitting for both functions, and therefore the variables found are not reliable. The same factors of discrepancy discussed for the background thermal-neutron count rate with the Am/Be neutron source are applicable here too, with the main difference being the much larger dimensions of the neutron cave containing the G-16 NG.

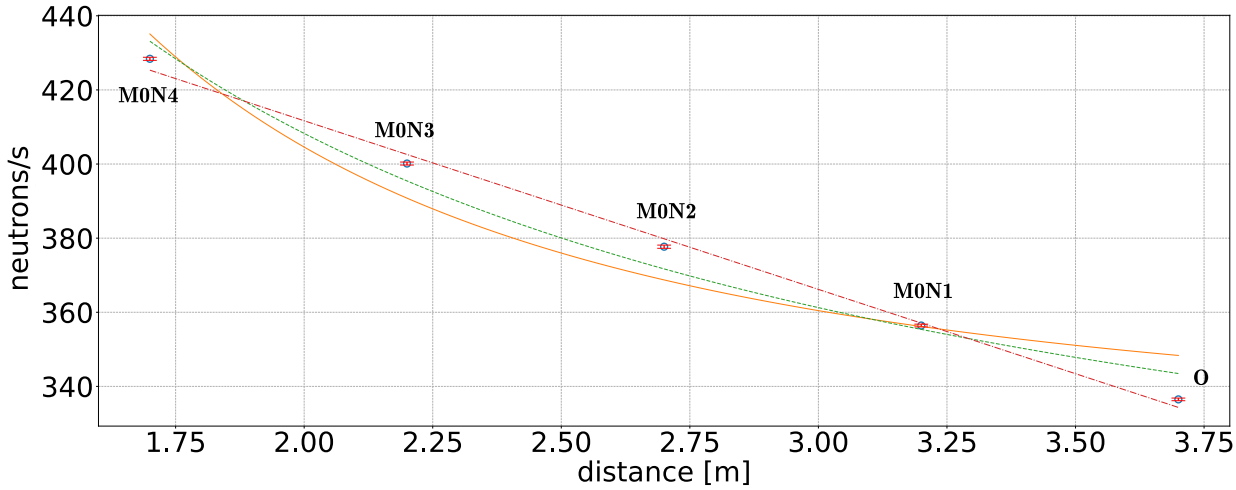

Figure 4.4: Neutrons/second as a function of distance from the G-16 NG, using the five positions on the first row of the grid. The points are hollow blue circles, with associated error bars in red. The point-source fit is represented by the orange line, while the linear-source fit is represented by the green, dashed line. The straight-line fit is represented by the burgundy, dash-dot line.

Ultimately, neither the point-source fit function nor the linear-source fit function provided an inverse-square law correspondence. To obtain such correspondence would require a fully-detailed and defined geometry of the laboratory space and experimental set-up, modelled in a Monte-Carlo simulation. In spite of this, a straight-line fit could be used to obtain a reasonable prediction of thermal-neutron count rate with varying direct source-to-detector distance. The straight-line fit was performed using:

$$y = mr + d. \tag{4.3}$$

The reduced chi-square value of Equation 4.3 was 39, which was an improvement of goodness of fit compared to the point-source and linear-source fit functions. The variables, however, do not carry any physical meaning. It should be noted that the measurement analysis performed did not take fast neutrons into account.

4.2 Gamma-ray Measurements

4.2.1 Gamma-ray Background and Background-Correction

Figure 4.5(a) shows the full background γ-ray spectrum with energy range up to 20 MeV, from the HPGe detector. After 3000 keV, no visible peaks were found, and contributions to the spectrum were mainly due to the cosmic ray background. Figure 4.5(b) zooms into the energy range 225-3000 keV of the background spectrum, where visible peaks are found. The peaks were identified using the decay radiation database derived from Nuclear Structure and Decay Data (NuDat 3.0), from the National Nuclear Data Center (NNDC) [12]. Most of the peaks belonged to the decay products of the ^{232}Th decay chain and ^{238}U decay chain. The presence of the parent isotopes of the three decay chains and ^{40}K were attributed to the natural radioactivity within building materials [45]. An exception, was the cosmogenic isotope ^{24}Na, which origins can be traced from cosmic ray interactions with the rocks and

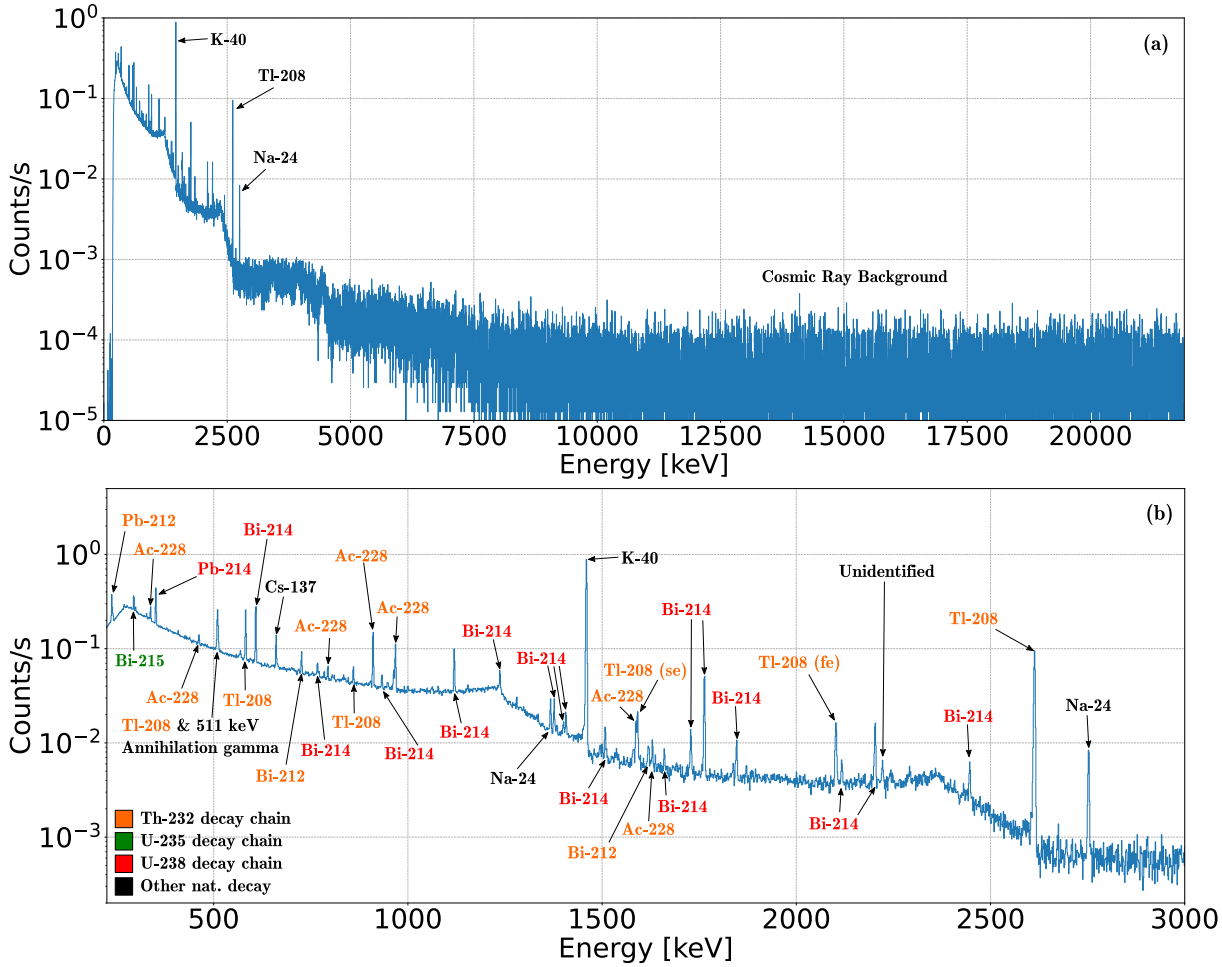

Figure 4.5: Background γ-ray spectrum recorded with the HPGe detector, bin width is 1.34 keV. (a) Full spectrum from 0 to 22 MeV, with prominent features labelled. (b) Range covering only 225 to 3000 keV, the identified isotopes are colour-coded to differentiate between decay chains.

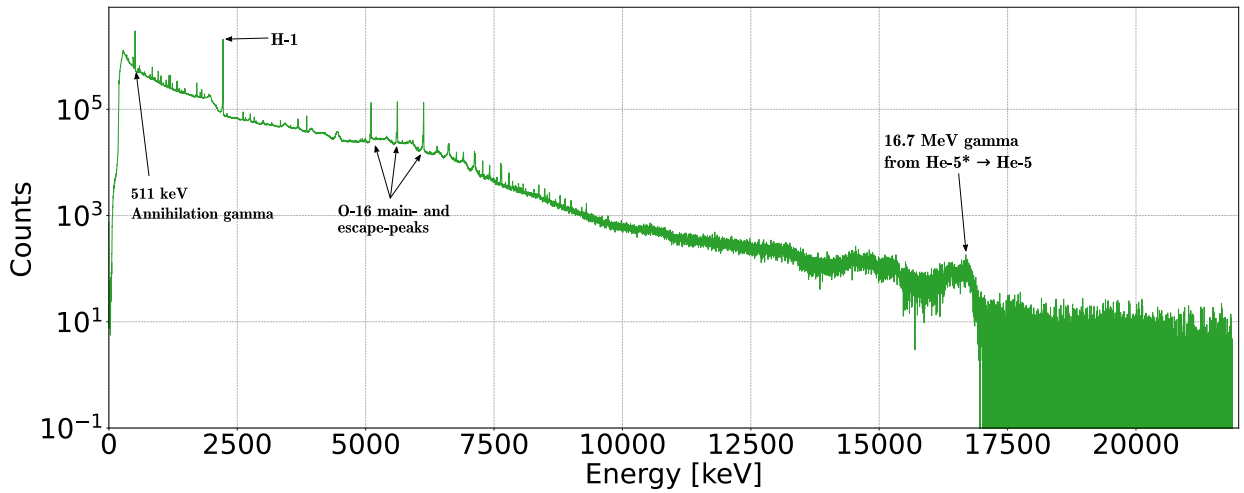

Figure 4.6: Full background-corrected γ-ray spectrum with bin width of 1.34 keV. Prominent features are identified.

soil on Earth. There was also a peak (another peak not featured in Figure 4.5(b)) marked as “Unidentified" as the list of potential isotopes with the corresponding γ-ray energy from the decay radiation database was unlikely to be present in the laboratory space.

Figure 4.6 shows the total counts of the entire background-corrected γ-ray spectrum, with an energy range from 0 to 22 MeV from the HPGe detector. As there are many peaks in the spectrum, owing to the high resolution of the detector, the spectrum was divided for the purposes of presentation. The energy range from 225 keV to 10 MeV will be discussed in further detail in Section 4.2.2, and the energy range from 10 to 22 MeV in Section 4.2.3. Many of the γ-ray peaks are from the Ge isotopes from the detector itself, and Al isotopes from the detector housing. There are also contributions from the neutron and γ-ray shielding, such as H, O, B, C, and Pb isotopes. The liquid nitrogen used to cool down the detector also contributes some γ-ray peaks. In addition, the steel structures used for the neutron cave also contribute a variety of isotopes, such as Fe, Cu, Co, Si, etc. The γ-ray peaks from the spectrum were initially identified and labelled with the parent isotope from the Prompt Gamma-ray Neutron Activation Analysis (PGAA) database from the International Atomic Energy Agency (IAEA) [46]. A limitation of the PGAA database is that the γ-rays listed are from thermal-neutron capture reactions of the parent isotope, and only the thermal-neutron cross section is provided, without the relative intensity or reaction process that produces each γ-ray. To supplement the PGAA database, several of the γ-rays emitted from fast-neutron induced reactions with the isotopes ^{27}Al, ^{56}Fe, ^{72}Ge, ^{74}Ge, and ^{208}Pb were identified. The γ-rays were identified from the Evaluated Nuclear Structure Data File (ENSDF) [47], and other relevant literature. For energies above 10 MeV, γ-rays from the DT fusion reaction in the G-16 NG was identified, and is discussed in Section 4.2.3. Above 17 MeV no further peaks could be identified. All of the identified peaks from the background and background-corrected γ-ray spectrum are listed in Appendices A and B, respectively.

4.2.2 Gamma-rays from Neutron Activation

In each background-corrected part of the spectrum, prominent peaks are labelled. Fast-neutron induced reactions are labelled with the compact notation of the corresponding reaction. For energies above 1.022 MeV, where pair production is possible, the peaks and associated fe- and se-peaks are labelled. The peaks were identified with their relative intensity to the background, as well as their peak width. Broad peaks are identified by multiple isotopes that emit γ-ray energies within the full width at half maximum (FWHM) of the peak, but can also be from the consequence of nuclear recoil or other nuclear effects. It should be noted that most of the γ-rays are produced from the de-excitation of the daughter nucleus from thermal-neutron capture $^{A}X_{N}(n,\gamma)^{A+1}X^{*}_{N+1}$ reactions.

Figure 4.7 features the background-corrected spectrum from 225 to 1000 keV. This first part of the spectrum began at 225 keV as no identifiable peaks were present below this energy due to the low-energy threshold set to block noise in the DAQ chain. Numerous peaks from the activation of the Ge crystal in the HPGe detector, as well as isotopes from the local environment are identified. The broad peak at 477 keV is listed with multiple isotopes identified with the FWHM of the peak, but is mainly from the Doppler broadening of the ^{10}B(n,α)^{7}Li reaction, resulting in a width of ∼15 keV [48]. Another prominent feature is the 511 keV γ-ray from pair production, as discussed in Section 2.2.1. The broad, triangular peaks at ∼600 and ∼700 keV are also attributed to Ge recoil reactions (n,n'γ) from 14 MeV neutrons [7, 49, 50]. Additionally, the fast-neutron induced reaction ^{74}Ge(n,p)^{74}Ga, with

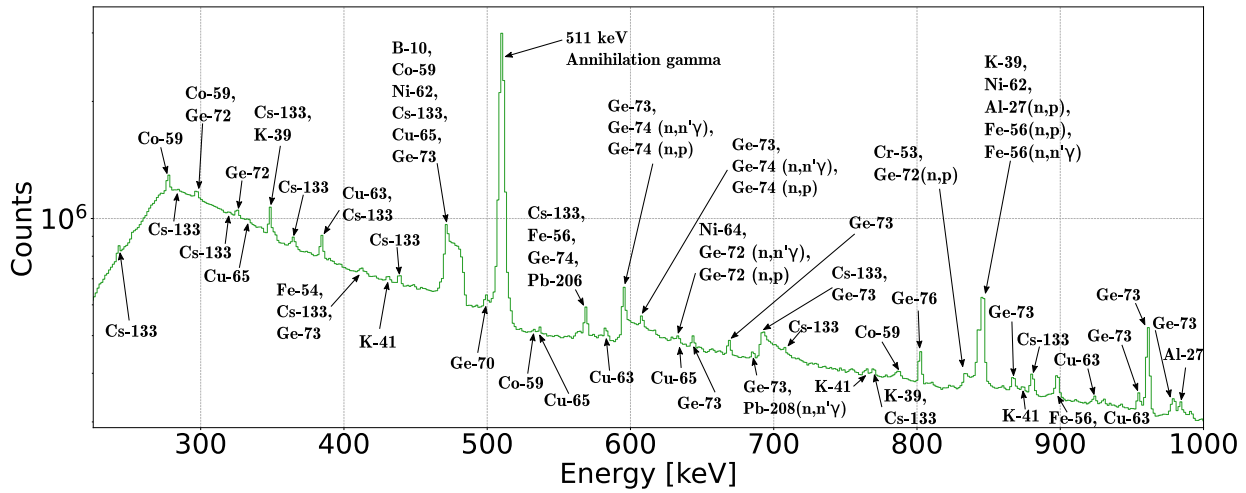

Figure 4.7: Magnification of background-corrected γ-ray spectrum from energy range 225 to 1000 keV with bin width of 1.34 keV.

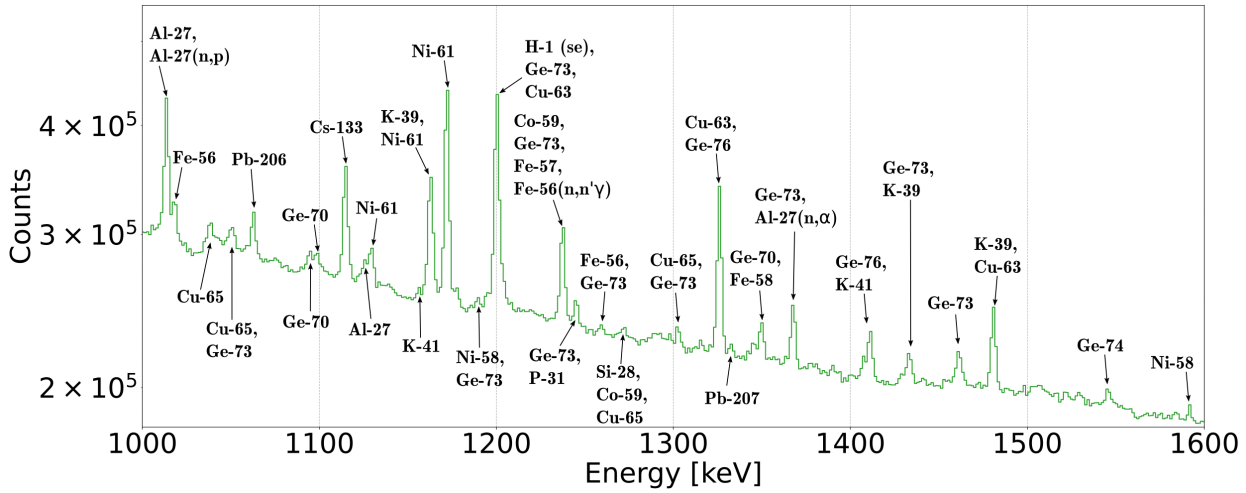

Figure 4.8: Magnification of background-corrected γ-ray spectrum from energy range 1000 to 1600 keV with bin width of 1.34 keV.

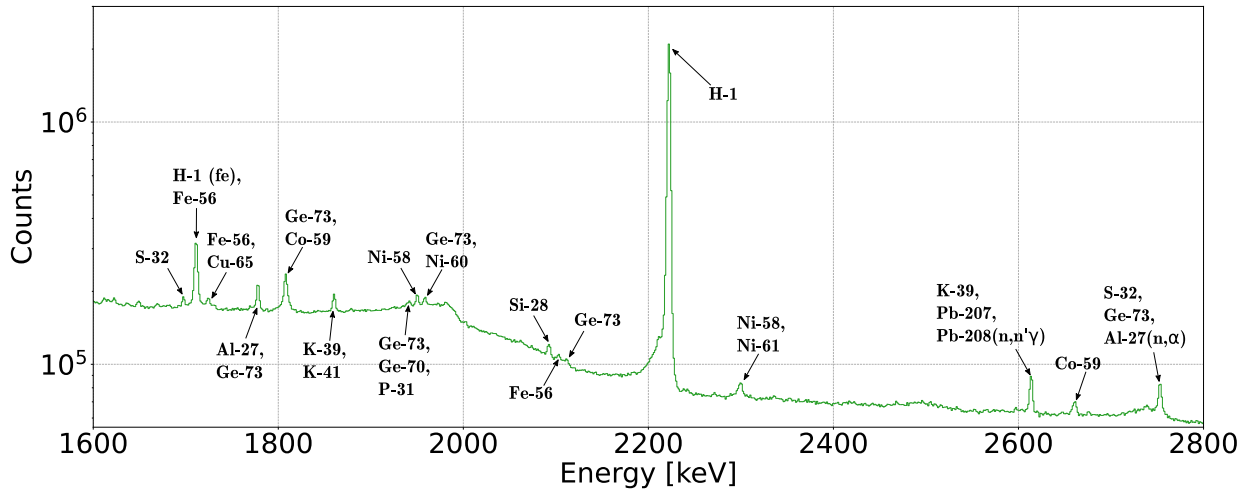

Figure 4.9: Magnification of background-corrected γ-ray spectrum from energy range 1600 to 2800 keV with bin width of 1.34 keV.

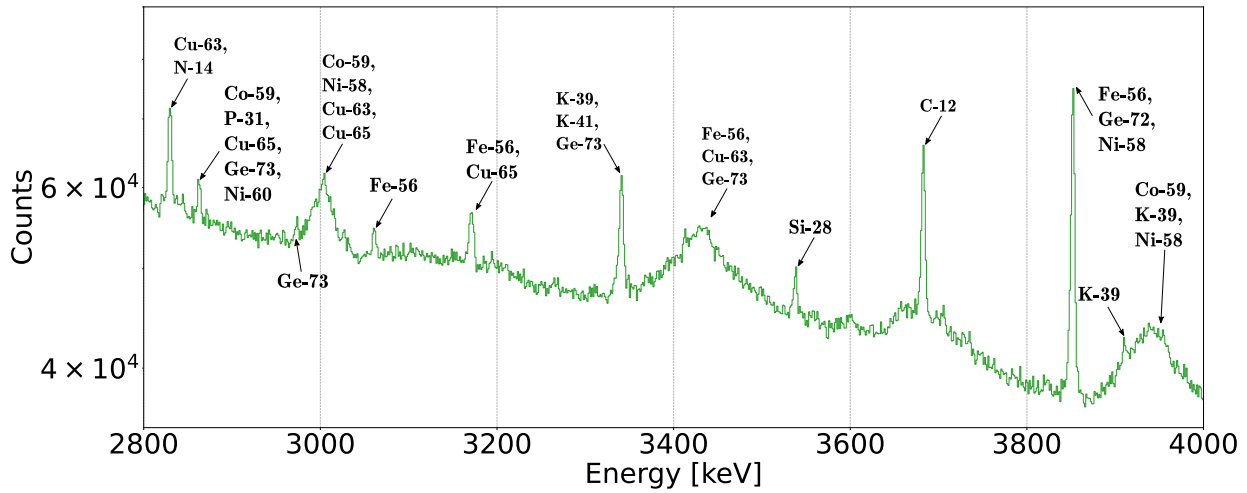

Figure 4.10: Magnification of background-corrected γ-ray spectrum from energy range 2800 to 4000 keV with bin width of 1.34 keV.

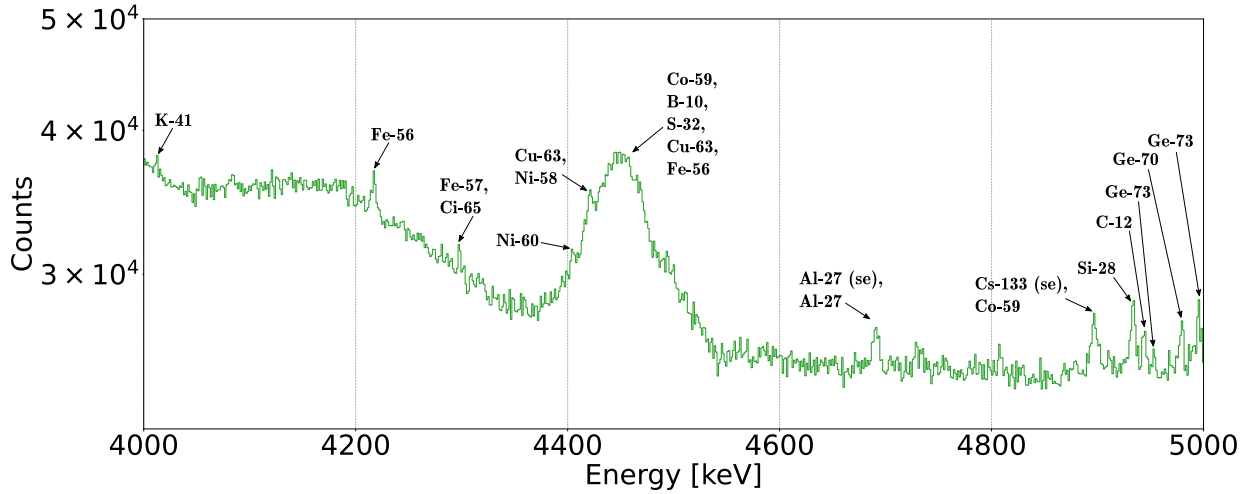

Figure 4.11: Magnification of background-corrected γ-ray spectrum from energy range 4000 to 5000 keV with bin width of 1.34 keV.

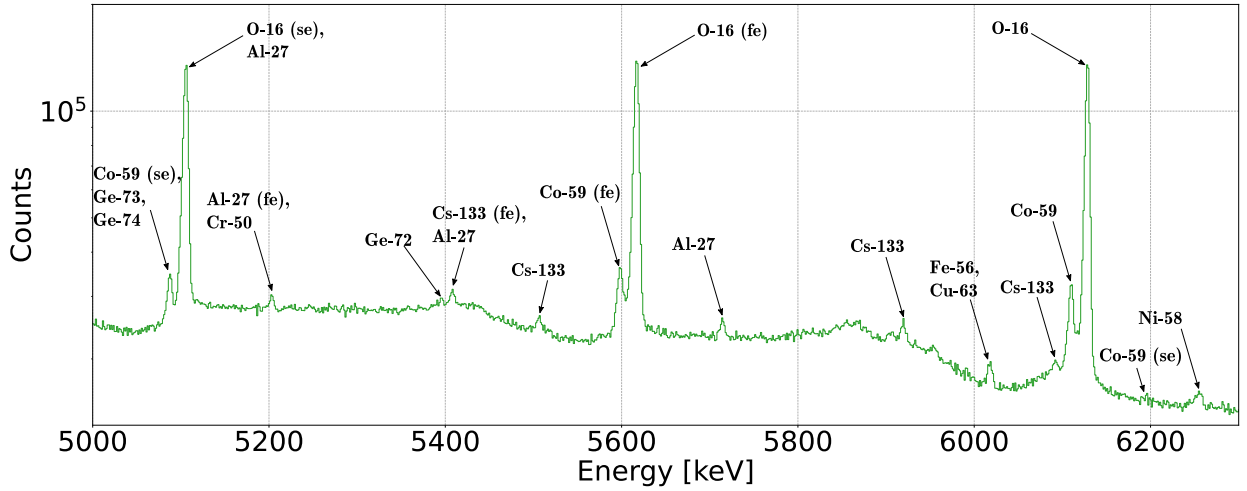

Figure 4.12: Magnification of background-corrected γ-ray spectrum from energy range 5000 to 6300 keV with bin width of 1.34 keV.

^{74}Ga β^--decaying back to ^{74}Ge also contributed to the peak at ∼600 keV [51, 52]. Similarly, the peak at ∼608 keV was also contributed to by ^{74}Ge(n,n'γ) and ^{74}Ge(n,p)^{74}Ga reactions. The peak at ∼630 keV was contributed to by fast-neutron induced reactions of ^{72}Ge(n,n'γ) and ^{72}Ge(n,p)^{72}Ga, with ^{72}Ga β^--decaying back to ^{72}Ge [53, 54, 55]. Inelastic scattering by fast-neutrons of ^{208}Pb(n,n'γ) contributed to the peak at ∼680 keV [56]. The ^{72}Ge(n,p)^{72}Ga fast-neutron induced reaction may also have contributed to the peak at ∼830 keV. There are three different fast-neutron induced reactions that contributed to the peak at ∼845 keV: ^{27}Al(n,p)^{27}Al, with ^{27}Al β^--decaying back to ^{27}Al [57, 58]; ^{56}Fe(n,p)^{56}Mn, with ^{56}Mn β^--decaying back to ^{56}Fe [59, 60]; and ^{56}Fe(n,n'γ) [61].

Figure 4.8 covers the spectrum from 1000 to 1600 keV. In this part of the spectrum, γ-rays from activation of Ge crystals are also observed, as well as activation of isotopes from the steel structure of the neutron cave. Additionally, γ-rays from activation of the lead shielding in front of the detector was observed at ∼1060 keV and ∼1332 keV. Above energies of 1.022 MeV, pair production is possible, and therefore fe- and se-escape peaks are observed, as discussed in Section 2.2.2. The se-peak observed at 1200 keV is from ^{1}H, and the associated fe- and main-peaks are featured in the next part of the spectrum in Figure 4.9. In addition, ^{73}Ge and ^{63}Cu were also included with the se-peak of ^{1}H, as they have γ-rays within the FWHM energy range of the peak. The fast-neutron induced reaction ^{27}Al(n,p)^{27}Mg was also found to have contributed to the peak at ∼1015 keV. The peak at ∼1240 keV was contributed to by ^{56}Fe(n,n'γ). At the peak ∼1370 keV, there was also contribution from the fast neutron-induced reaction ^{27}Al(n,α)^{24}Na, with ^{24}Na β^--decaying to ^{24}Mg [56, 62].

The spectrum from 1600 to 2800 keV is shown in Figure 4.9. The most prominent feature in this part of the spectrum is from the thermal-neutron capture reaction ^{1}H(n,γ)^{2}H*, whereby the de-excitation of ^{2}H produces a γ-ray contributing to ∼2222 keV [63, 64, 65, 66]. Additionally, γ-rays from the Ge crystal in the HPGe detector, isotopes of the steel structure, lead shielding, and K, were observed. The peak at ∼2615 keV was contributed to by inelastic scattering of fast-neutrons with ^{208}Pb(n,n'γ). The ^{27}Al(n,α)^{24}Na reaction also contributed to the peak at ∼2755 keV. Figure 4.10 covers the spectrum from 2800 to 4000 keV. Several sharp peaks are identified that are a combination of multiple isotopes, with the exception of the single ^{12}C peak at ∼3682 keV. The peak at ∼3850 keV with ^{56}Fe, ^{72}Ge, and ^{58}Ni was also observed to have a fe-peak and se-peak at ∼3340 keV and ∼2830 keV, respectively. Additionally, the wide, triangular peak at ∼3940 keV with ^{59}Co, ^{39}K, and ^{58}Ni, and at ∼3430 keV with ^{56}Fe, ^{63}Cu, and ^{73}Ge, were identified to be escape peaks from the peak at ∼4450 keV in Figure 4.11.

The spectrum from 4000 to 5000 keV is shown in Figure 4.11. This part of the spectrum features multiple peaks from the isotopes of the neutron cave, HPGe detector, and the surrounding laboratory concrete walls. The wide, triangular peak at ∼4450 keV is identified with a variety of isotopes, but is presented with five isotopes with the highest relative thermal-neutron cross section. As mentioned at the end of Section 4.2.1, the relative intensity of each γ-ray was not provided by the PGAA database, hence the isotopes that are the main contributors to the wide peak is not known. Another contributor to the triangular peaks at ∼4450 keV, and even ∼3000 keV, ∼3430 keV and ∼3940 keV in Figure 4.10 could be due to fast-neutron induced recoil effects. The exact cause of these triangular peaks require further investigation. Also identified are the se-peaks of ^{27}Al and ^{133}Cs, of which the fe- and main-peaks are labelled in Figure 4.12.

Figure 4.12 covers the spectrum from 4000 to 5000 keV. The fe- and main-peak of ^{27}Al is observed at ∼5200 keV and ∼5710 keV. The fe- and main-peak of ^{133}Cs is observed at ∼5410 keV and ∼5918 keV. The se-peak of ^{59}Co was identified at ∼6190 keV. The main and escape peaks of ^{16}O is observed at ∼5100 keV, ∼5617 keV, and ∼6128 keV. Two possible reaction processes give rise to the γ-ray of ^{16}O: inelastic scattering of ^{16}O(n,n')^{16}O*; and neutron capture ^{15}N(n,γ)^{16}N, followed by β^- decay to ^{16}O*. The cross-section of inelastic scattering process at neutron energy of 14 MeV is 0.309 b, as compared to 8.6 µb of the neutron capture process. The cross-section values were obtained from the ENDF/B-VIII.0 data library [44]. The absolute intensity of the 6128 keV γ-ray is 67% [67], which explains the high counts observed in the spectrum. Another factor is the abundance of ^{16}O present in the distilled water surrounding the neutron cave, in which inelastic scattering would occur with the fast neutrons emitted from the G-16 NG.

The spectrum from 6300 to 7000 keV is shown in Figure 4.13. The peaks of ^{72}Ge, ^{59}Co, and ^{204}Pb were identified. The escape peaks of several isotopes were also identified, where their associated main-peaks are identified in Figure 4.14. Some of the escape peaks were also observed to have higher counts than the main-peaks, due to a reduced probability of full-energy absorption by the HPGe detector. An example is the ^{73}Ge main-, fe-, and se-peaks at ∼7631, ∼7120, and ∼6608 keV, respectively. The corresponding counts are 9714, 16319, and 21515, while the cross sections are 0.779 mb, 0.882 mb, and 1.061 mb. The decrease in counts from the se-peak to the main-peak are attributed to the decrease in cross-section, and therefore escape peaks may be used to identify and determine the associated main-peak [28].

Another observation was the slight broadening of the fe-peak as compared to the main- and se-peaks. Taking the widths of the peaks of ^{32}S as an example; the main-, se-, and fe-peaks are at ∼7790, ∼7279 and ∼6767 keV, as presented in Figures 4.13 and 4.14. The widths of the main- and se-peaks is 14 keV, but the fe-peak is instead 17 keV. This phenomenon is caused from the momentum possessed by the electron-positron pair before annihilation, in which the momentum is not transferred equally to the pair of γ-rays, resulting in one γ-ray to have a slightly higher energy than the other. Therefore two different γ-ray energies contribute to the resultant fe-peak, leading to a slight broadening of the peak width [28, 68].

Figure 4.15 features the spectrum from 8010 to 9000 keV. Here, the main, and associated fe- and se-peaks of various isotopes are observed. An observation was that the counts of the peaks at this energy range, when compared to lower energies such as in Figure 4.9, is about two magnitudes lower. This can be attributed to the response function of the HPGe detector, where the γ-ray energies above 6 MeV are not fully-absorbed (photoelectric absorption) by the detector, and instead multiple Compton scatterings occur before photoelectric absorption, resulting in lower counts. [28, 69].

The spectrum from 9 to 10 MeV is presented in Figure 4.16. For energies above 9 MeV, the statistics drop enough such that the bin width had to be doubled to 2.67 keV/bin in order to identify peaks. Only three peaks were identified: the fe-peak of ^{53}Cr; ^{54}Fe; and main-peak ^{53}Cr.

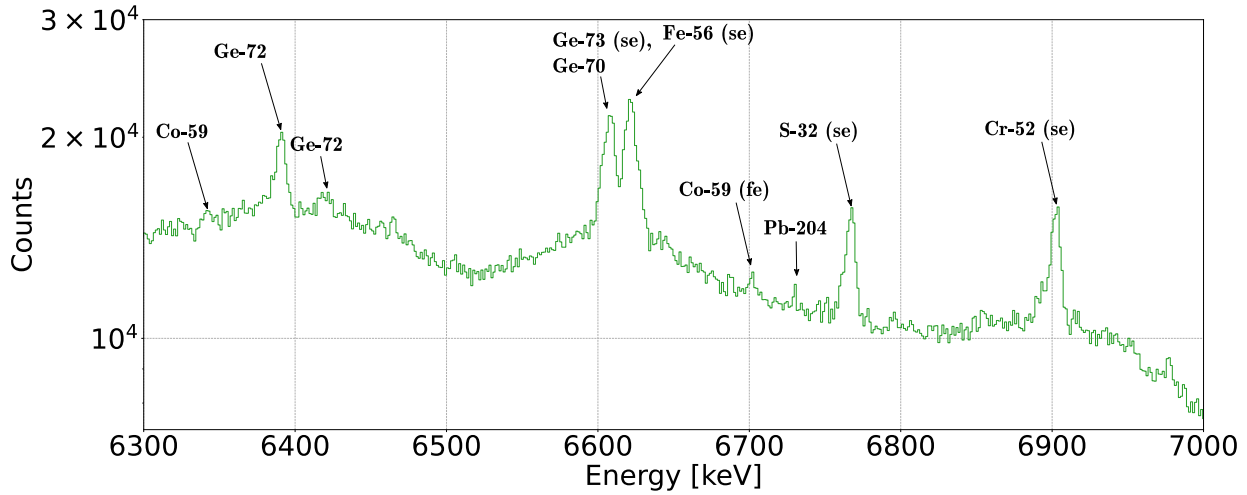

Figure 4.13: Magnification of background-corrected γ-ray spectrum from energy range 6300 to 7000 keV with bin width of 1.34 keV.

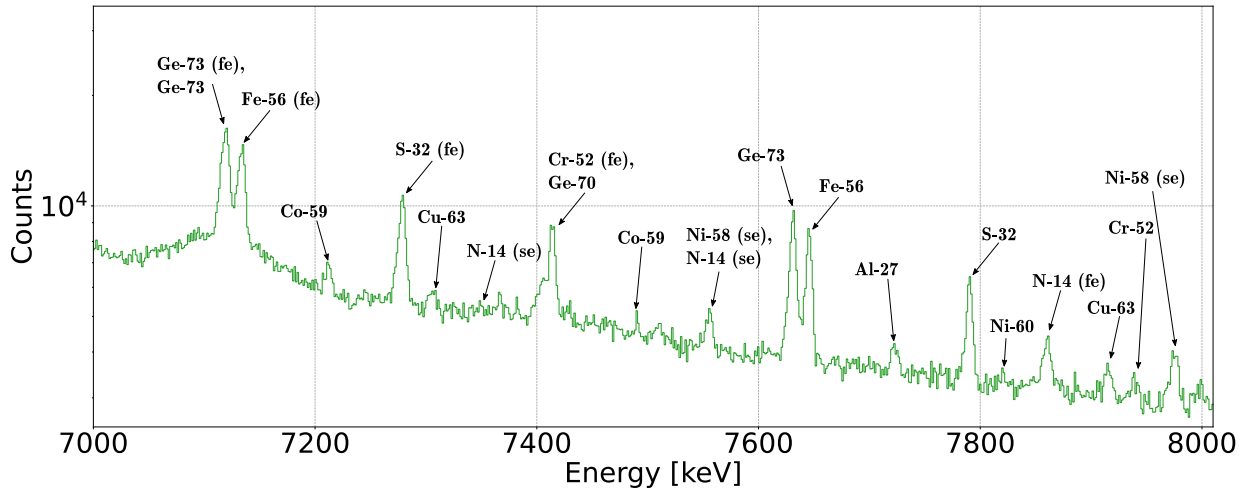

Figure 4.14: Magnification of background-corrected γ-ray spectrum from energy range 7000 to 8010 keV with bin width of 1.34 keV.

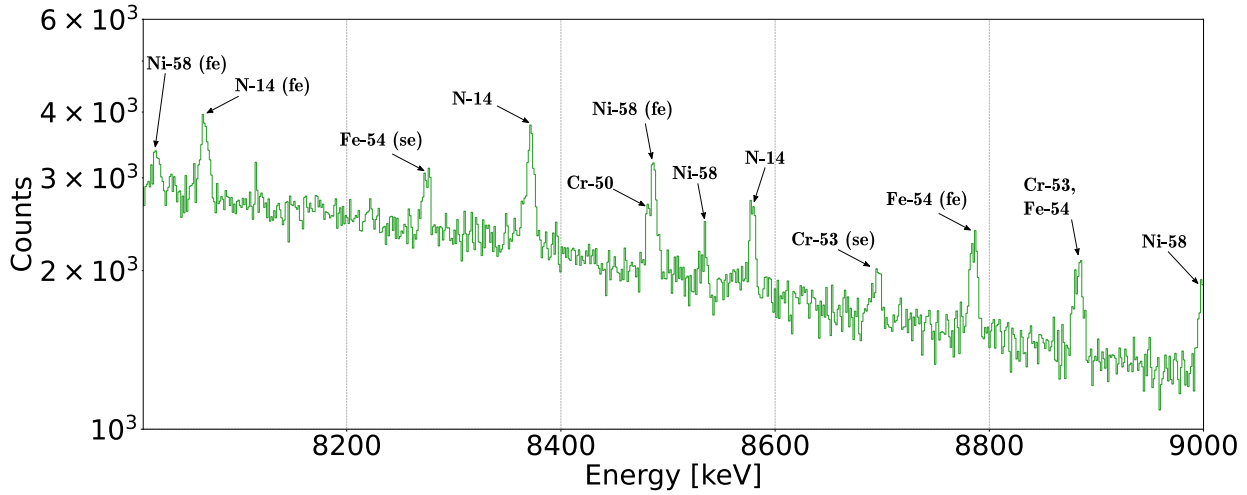

Figure 4.15: Magnification of background-corrected γ-ray spectrum from energy range 8010 to 9000 keV with bin width of 1.34 keV.

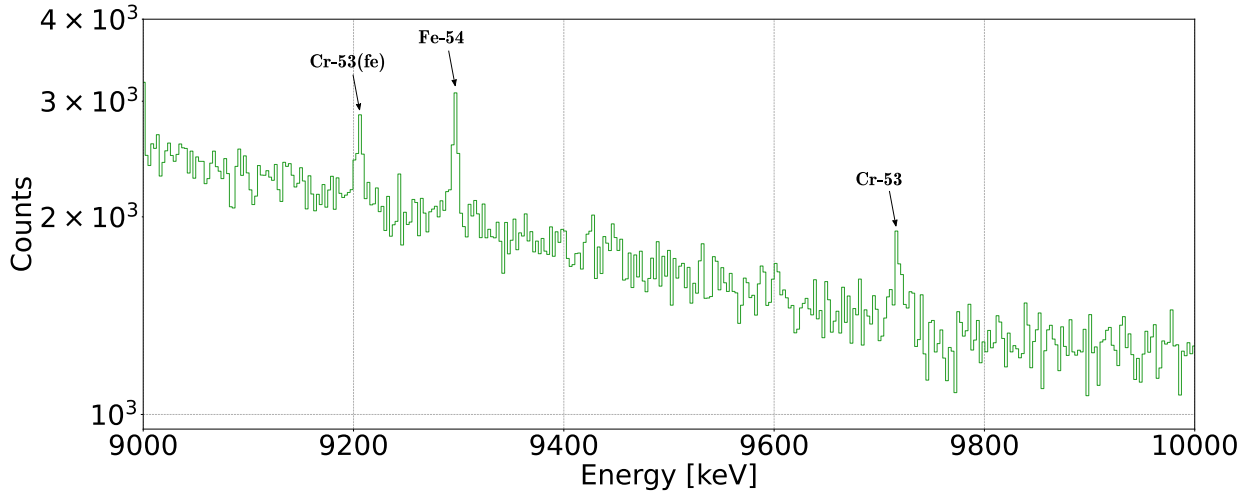

Figure 4.16: Magnification of background-corrected γ-ray spectrum from energy range 9 to 10 MeV with bin width of 2.67 keV.

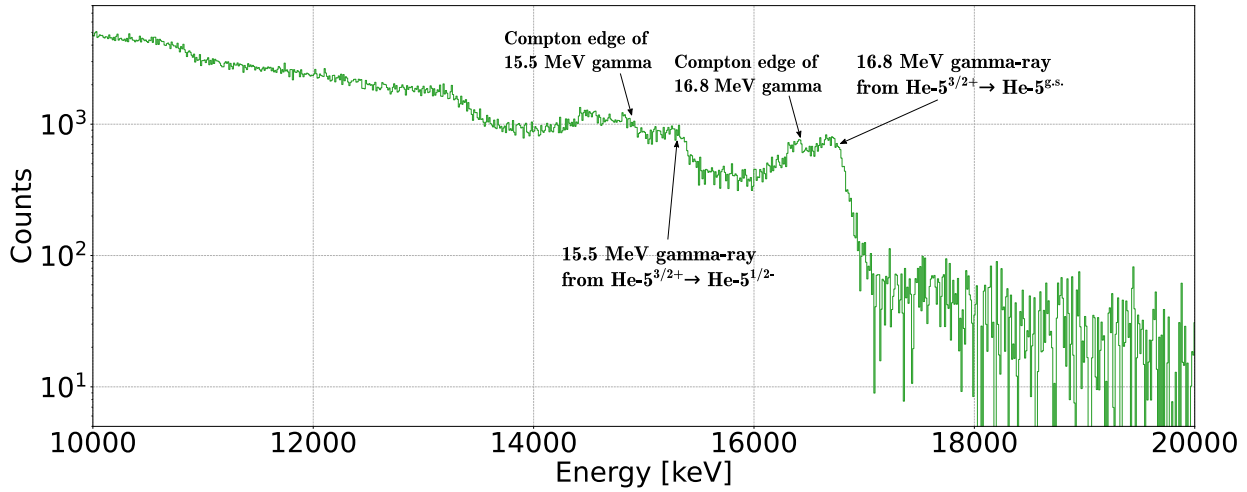

Figure 4.17: Magnification of background-corrected γ-ray spectrum from energy range 10 to 20 MeV with bin width of 10.64 keV.

4.2.3 Gamma-rays from Neutron Generator

Figure 4.17 features the spectrum from 10 to 20 MeV, with the bin width adjusted to 10.68 keV/bin. Here, the γ-rays from the DT fusion reaction from the G-16 NG are observed, as discussed in Section 2.1.4. Owing to the small branching ratio, the ^{3}H(d,γ)^{5}He reaction is less likely to occur than the ^{3}H(d,n)^{4}He reaction. Nevertheless, the γ-rays from the de-excitation of the product nucleus ^{5}He was observed. Two γ-rays, and their associated Compton edges (Section 2.2.2), are labelled in Figure 4.17. There are twelve known excited states of ^{5}He, from Table 5.1 of [70]. The energy level scheme shown in Figure 4.18 features only the ground state and the first two excited states of ^{5}He, which were observed in the present work. The 16.8 MeV γ-ray corresponds to the de-excitation from the second excited state ($\mathbf{J}^{\pi} = 3/2^{+}$) to the ground state ($\mathbf{J}^{\pi} = 3/2^{-}$), while the 15.5 MeV γ-ray corresponds to the de-excitation from the second excited state to first excited state ($\mathbf{J}^{\pi} = 1/2^{-}$).

In general, γ-ray transitions between energy states obey an angular momentum and parity

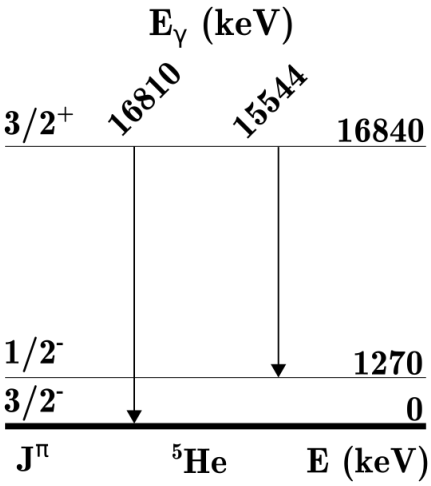

Figure 4.18: Energy level scheme of ^{5}He. The angular momentum and parity quantum numbers J^π are shown on the left, and the energy levels of the ground state and first two excited states on the right. The energy of emitted γ-rays from de-excitation of ^{5}He is shown in the middle.

selection rule: the difference between initial and final angular momentum and parity separate the transition into electric transitions or magnetic transitions [22]. The emission probability of electric transitions are higher than magnetic transitions, therefore the two γ-ray electric transitions shown in Figure 4.18 are observed in the spectrum. Potential work would be to utilise these energetic γ-rays from a G-16 NG for neutron TOF studies.

5 Summary and outlook

This thesis has detailed the work undertaken at the Nuclear Applications Laboratory at Lund University, to expand the use of sources of free neutrons for a multitude of research and educational purposes. The G-16 NG is an example of a source of free neutrons, which this project is centred around. The use of the G-16 NG was extended beyond its existing application to NAA, by re-configuring the neutron cave containing the G-16 NG for both purposes of irradiating samples internally, and extracting fast neutrons. Following the re-configuration, measurements of both thermal neutrons and γ-rays when the neutron cave is in fast-neutron extraction mode were performed. Finally, γ-rays emitted from neutron activation of the objects around the laboratory space were identified, as well as the fusion reactions from the G-16 NG in the neutron cave. The PGAA database, ENSDF, and other relevant literature were used in the identification of the γ-rays emitted.

5.1 Attainment of Project Goals and Statement of Key Findings

The project goals were attained as enumerated below, where each point corresponds to the project goals stated in Section 1.2.

1. To reconfigure the neutron cave, the neutron box containing the G-16 NG was placed atop a turntable assembly with additional neutron shielding. Next, a collimated exit port to guide the fast neutrons outside the neutron cave was also built.

2. Thermal neutron measurements were taken at 15 positions corresponding to the detector placement grid using a ^{3}He PC. The analysis of the measurement in direct line-of-sight of the G-16 NG yielded a fitting function that provides a reasonable prediction of the thermal-neutron count rate.

3. γ-ray measurements were obtained at one of the position of the grid, in direct line-of-sight using a HPGe detector. The analysis of the background and background-corrected γ-ray spectrum yielded identification of γ-rays from thermal-neutron capture reactions, and fast-neutron induced reactions.

4. Two γ-rays from DT fusion reaction of the G-16 NG were identified, which could serve as potential candidates for neutron TOF measurements.

The major findings are as listed:

- There was a gap in the shielding of the neutron cave which allowed for neutrons to escape.

- The measurements of thermal-neutrons could be validated by fitting an inverse-square function to the background Am/Be neutron source measurements.
- The straight-line fit function (Equation 4.3) can be used to predict thermal-neutron count rate within reasonable confidence for direct line-of-sight source-to-detector distances.
- The lead and polyethylene wall built in front of the HPGe detector can be utilised for dead time reduction when taking measurements with the G-16 NG turned on.
- A wide variety of natural radioisotopes within building materials were identified from the background γ-ray spectrum from the HPGe detector.
- Thermal-neutron capture reactions of materials found in the laboratory space resulting in emission of γ-rays were identified.
- Selected isotopes resulting in the emission of γ-rays from fast-neutron induced reactions were identified.
- γ-rays from the fusion reaction $^{3}\mathrm{H(d,\gamma)}^{5}\mathrm{He}$ from a G-16 NG were identified using the HPGe detector. The γ-ray energies are 16.8 MeV and 15.5 MeV.

5.2 Future Work

The recommended future work is listed below:

1. The sealing of the gap in the shielding of the neutron cave is the first recommendation for future work. The reduction of neutrons escaping the neutron cave will not only improve measurements, abut also reduce neutron dosage to users.
2. The modelling of the described laboratory space and experimental set-up in a fully-detailed Monte-Carlo simulation would allow for an improved prediction of neutron flux outside the neutron cave.
3. To use the energetic 16.8 MeV and 15.5 MeV γ-rays from the DT fusion reaction in the G-16 NG as a trigger for neutron tagging using the TOF method. Development in this direction could allow for better characterisation of the fast neutrons from the G-16 NG.
4. Further analysis of the γ-ray spectrum obtained from the HPGe detector. The peaks could be, for example, Gaussian-fitted, allowing for verification of the identified peaks. The relative intensity of each γ-ray should also be cross-checked, as well as the identification of the nuclear reaction yielding each γ-ray.

Acknowledgements

I would like to first thank my supervisor, Robert Frost, for his constant guidance during the entirety of the project, and for encouraging me to work independently instead of simply giving out the answer. I also thank him for challenging me throughout the project, from experimental work, to the writing of this thesis; without which I would not have learnt as much as I have.

I would also like to thank several people in the Nuclear Physics department for their guidance and advice. To Nicholai Mauritzson, for getting me started with the project by giving me a crash-course on detectors and spectrum features, but also being another resource for when I have questions. To Kevin Fissum, for his insight, and patience in making sure I understand the conversations between him and Nicholai. To Mikael Elfman, for giving me advice with the experimental set-up, and for getting me acquainted with the MAESTRO software. And lastly, to Cornelius Maurer, for helping me out with data acquisition of the HPGe detector.

References

[1] S. A. E. Johansson, T. B. Johansson. Analytical application of particle induced X-ray emission. *Nuclear Instruments and Methods*, vol. 137 (1976), 473–516. doi:10.1016/0029-554X(76)90470-5

[2] R. J. W. Frost, N. De La Rosa, M. Elfman, *et al.* One detector, all the light elements – Low-background NRA, RBS and ERDA for the quantification of elements from hydrogen to fluorine. *Nuclear Instruments and Methods in Physics Research Section B: Beam Interactions with Materials and Atoms*, vol. 494-495 (2021), 34–45. doi:10.1016/j.nimb.2021.02.009

[3] C. Bernhardsson, K. Stenström, M. Jönsson, *et al. Assessment of "Zero Point" radiation around the ESS facility.* MA RADFYS 2018:01. Lund University (2019)

[4] H. Perrey, M. Elfman, K. Fissum, *et al.* From micro- to macro- neutron sources: The Lund Broad-band Neutron Facility. *EPJ Web of Conferences*, vol. 231 (2020), 01005. doi:10.1051/epjconf/202023101005

[5] B. Seitz, J. R. M. Annand, L. Boyd, K. Fissum. Modern Neutron Detectors with Fast Timing Resolution. Tech. Rep. IAEA-TECDOC–1935, International Atomic Energy Agency (2020)

[6] H. Perrey, L. Ros, M. Elfman, *et al.* Evaluation of the in-situ performance of neutron detectors based on EJ-426 scintillator screens for spent fuel characterization. *Nuclear Instruments and Methods in Physics Research Section A: Accelerators, Spectrometers, Detectors and Associated Equipment*, vol. 1020 (2021), 165886. doi:10.1016/j.nima.2021.165886

[7] J. Lindsey-Clark. Development of a neutron activation analysis station at the Lund Ion Beam Analysis Facility. Student Paper, Department of Physics, Lund University (2021). URL `lup.lub.lu.se/student-papers/record/9038694`

[8] F. Messi, H. Perrey, K. Fissum, *et al.* The Neutron-Tagging Facility at Lund University. Tech. Rep. IAEA-TECDOC–1935, International Atomic Energy Agency (2020)

[9] E. Rutherford. LIV. Collision of α particles with light atoms. IV. An anomalous effect in nitrogen. *The London, Edinburgh, and Dublin Philosophical Magazine and Journal of Science*, vol. 37 (1919), 581–587. doi:10.1080/14786440608635919

[10] J. Chadwick. The existence of a neutron. *Proceedings of the Royal Society of London. Series A, Containing Papers of a Mathematical and Physical Character*, vol. 136 (1932), 692–708. doi:10.1098/rspa.1932.0112

[11] W. Pauli. Über den Zusammenhang des Abschlusses der Elektronengruppen im Atom mit der Komplexstruktur der Spektren. *Zeitschrift für Physik*, vol. 31 (1925), 765–783. doi:10.1007/BF02980631

[12] A. A. Sonzogni. NuDat 2.0: Nuclear Structure and Decay Data on the Internet (2005). doi:10.1063/1.1945075

[13] E. Rutherford. Discussion on the structure of atomic nuclei. *Proceedings of the Royal Society of London. Series A, Containing Papers of a Mathematical and Physical Character*, vol. 123 (1929), 373–390. doi:10.1016/b978-0-08-006630-1.50010-6

[14] C. F. v. Weizsäcker. Zur Theorie der Kernmassen. *Zeitschrift für Physik*, vol. 96 (1935), 431–458. doi:10.1007/BF01337700

[15] H. A. Bethe. Nuclear Physics B. Nuclear Dynamics, Theoretical. *Reviews of Modern Physics*, vol. 9 (1937), 69–244. doi:10.1103/RevModPhys.9.69

[16] A. Belyaev, D. Ross. *The Basics of Nuclear and Particle Physics*, chap. 3. Nuclear Masses and the Semi-Empirical Mass Formula, 37–52. Springer International Publishing, Cham (2021). ISBN 978-3-030-80116-8. doi:10.1007/978-3-030-80116-8_3

[17] K. S. Krane. *Introductory Nuclear Physics*, chap. 3. Nuclear Properties, 44–79. Wiley, New York, NY (1988)

[18] K. S. Krane. *Introductory Nuclear Physics*, chap. 6. Radioactive Decay, 160–191. Wiley, New York, NY (1988)

[19] A. Belyaev, D. Ross. *The Basics of Nuclear and Particle Physics*, chap. 5. Radioactivity, 67–88. Springer International Publishing, Cham (2021). ISBN 978-3-030-80116-8. doi:10.1007/978-3-030-80116-8_5

[20] W. R. Leo. *Techniques for Nuclear and Particle Physics Experiments*, chap. 2. Passage of Radiation Through Matter, 17–64. Springer, Berlin, Heidelberg (1994). doi:10.1007/978-3-642-57920-2

[21] B. Lehnert, M. Hult, G. Lutter, K. Zuber. Search for the decay of nature's rarest isotope ^{180m}Ta. *Physical Review C*, vol. 95 (2017), 044306. doi:10.1103/PhysRevC.95.044306

[22] K. S. Krane. *Introductory Nuclear Physics*, chap. 10. Gamma Decay, 327–377. Wiley, New York, NY (1988)

[23] A. Belyaev, D. Ross. *The Basics of Nuclear and Particle Physics*, chap. 4. The Nuclear Shell Model, 53–66. Springer International Publishing, Cham (2021). ISBN 978-3-030-80116-8. doi:10.1007/978-3-030-80116-8

[24] G. L. Morgan, P. W. Lisowski, S. A. Wender, *et al.* Measurement of the branching ratio ^{3}H(d,γ)/^{3}H(d,n) using thick tritium gas targets. *Physical Review C*, vol. 33 (1986), 1224–1227. doi:10.1103/PhysRevC.33.1224

[25] K. S. Krane. *Introductory Nuclear Physics*, chap. 14. Nuclear Fusion, 528–558. Wiley, New York, NY (1988)

[26] G. F. Knoll. *Radiation Detection and Measurement 4th ed.*, chap. 2. Radiation Interaction, IV: Interaction of Neutrons, 53–55. John Wiley & Sons, Inc. (2010)

[27] W. R. Leo. *Techniques for Nuclear and Particle Physics Experiments*, chap. 2. Passage of Radiation Through Matter, 17–64. Springer, Berlin, Heidelberg (1994). doi:10.1007/978-3-642-57920-2

[28] G. F. Knoll. *Radiation Detection and Measurement 4th ed.*, chap. 12. Germanium Gamma-Ray Detectors, 415–466. John Wiley & Sons, Inc. (2010)

[29] W. R. Leo. *Techniques for Nuclear and Particle Physics Experiments*, chap. 10. Semiconductor Detectors, 207–240. Springer, Berlin, Heidelberg (1994). doi:10.1007/978-3-642-57920-2

[30] K. S. Krane. *Introductory Nuclear Physics*, chap. 7. Detecting Nuclear Radiations, 192–245. Wiley, New York, NY (1988)

[31] D. Reilly, N. Ensslin, H. J. Smith. Passive nondestructive assay of nuclear materials. Tech. Rep. NUREG/CR–5550, Los Alamos National Laboratory, United States (1991)

[32] G. F. Knoll. *Radiation Detection and Measurement 4th ed.*, chap. 14. Slow Neutron Detection Methods, 519–552. John Wiley & Sons, Inc. (2010)

[33] G. F. Knoll. *Radiation Detection and Measurement 4th ed.*, chap. 1. Radiation Sources, V: Neutron Sources, 19–26. John Wiley & Sons, Inc. (2010)

[34] K. S. Krane. *Introductory Nuclear Physics*, chap. 12. Neutron Physics, 444–477. Wiley, New York, NY (1988)

[35] *Neutron Generators for Analytical Purposes*. No. 1 in Radiation Technology Reports. International Atomic Energy Agency, Vienna (2012). ISBN 978-92-0-125110-7

[36] J. Verbeke, K. Leung, J. Vujic. Development of a sealed-accelerator-tube neutron generator. *Applied Radiation and Isotopes*, vol. 53 (2000), 801–809. doi:10.1016/S0969-8043(00)00262-1

[37] J. M. Carpenter, C.-K. Loong. *Elements of Slow-Neutron Scattering: Basics, Techniques, and Applications*, chap. 8. Detectors, 281–314. Cambridge University Press (2015). doi:10.1017/CBO9781139029315.011

[38] J. S. E. Townsend. IV. The diffusion of ions into gases. *Philosophical Transactions of the Royal Society of London. Series A, Containing Papers of a Mathematical or Physical Character*, vol. 193 (1900), 129–158. doi:10.1098/rsta.1900.0004

[39] W. R. Leo. *Techniques for Nuclear and Particle Physics Experiments*, chap. 6. Ionization Detectors, 119–148. Springer, Berlin, Heidelberg (1994). doi:10.1007/978-3-642-57920-2

[40] G. F. Knoll. *Radiation Detection and Measurement 4th ed.*, chap. 6. Proportional Counters, 159–206. John Wiley & Sons, Inc. (2010)

[41] S. Tavernier. *Experimental Techniques in Nuclear and Particle Physics*, chap. 4. Detectors Based on Ionisation in Gases, 105–142. Springer Berlin Heidelberg (2010). doi:10.1007/978-3-642-00829-0

[42] C. Bedouet, B. Vernet. *Genie 16NG User Manual*. Sodern (2014)

[43] J. Hubbell, S. Seltzer. *Tables of X-Ray Mass Attenuation Coefficients and Mass Energy-Absorption Coefficients (version 1.4). [Online] http://physics.nist.gov/xaamdi [Accessed: 2022-01-06]*. National Institute of Standards and Technology, Gaithersburg, MD. (2004)

[44] D. Brown, M. Chadwick, R. Capote, *et al.* ENDF/B-VIII.0: The 8th Major Release of the Nuclear Reaction Data Library with CIELO-project Cross Sections, New Standards and Thermal Scattering Data. *Nuclear Data Sheets*, vol. 148 (2018), 1–142. doi:10.1016/j.nds.2018.02.001

[45] R. Trevisi, F. Leonardi, S. Risica, C. Nuccetelli. Updated database on natural radioactivity in building materials in Europe. *Journal of Environmental Radioactivity*, vol. 187 (2018), 90–105. doi:10.1016/j.jenvrad.2018.01.024

[46] *Database of Prompt Gamma Rays from Slow Neutron Capture for Elemental Analysis*. Non-serial Publications. International Atomic Energy Agency, Vienna (2007). ISBN 92-0-101306-X

[47] M. R. Bhat. Evaluated Nuclear Structure Data File (ENSDF), In *Nuclear Data for Science and Technology*, 817–821. Springer, Berlin, Heidelberg (1992). doi:10.1007/978-3-642-58113-7_227

[48] J. L. Campbell, P. O'Brien, I. K. Mackenzie. An Undergraduate Experiment on Nuclear Lifetime Measurement Using the Doppler Effect. *American Journal of Physics*, vol. 40 (1972), 9–15. doi:10.1119/1.1986434

[49] M. Baginova, P. Vojtyla, P. P. Povinec. Investigation of neutron interactions with Ge detectors. *Nuclear Instruments and Methods in Physics Research Section A: Accelerators, Spectrometers, Detectors and Associated Equipment*, vol. 897 (2018), 22–31. doi:10.1016/j.nima.2018.04.036

[50] Y. G. Kosyak, L. V. Chekushina, A. S. Ermatov. Spins and lifetimes of ^{74}Ge levels from (n, n'γ) reactions. *Bulletin of the Russian Academy of Sciences: Physics*, vol. 67 (2003), 151

[51] H. W. Taylor, R. L. Schulte, P. J. Tivin, H. Ing. The Decay of 8.0 Min ^{74}Ga. *Canadian Journal of Physics*, vol. 53 (1975), 107–116. doi:10.1139/p75-016

[52] D. C. Camp, D. R. Fielder, B. P. Foster. Energy levels in ^{74}Ge from the decay of ^{74}Ga. *Nuclear Physics A*, vol. 163 (1971), 145–160. doi:10.1016/0375-9474(71)90526-4

[53] K. C. Chung, A. Mittler, J. D. Brandenberger, M. T. McEllistrem. Ge(n,n'γ) Reactions and Low-Lying States of Ge Isotopes. *Physical Review C*, vol. 2 (1970), 139–148. doi:10.1103/PhysRevC.2.139

[54] D. C. Camp. Energy levels in ^{72}Ge from the decays of ^{72}Ga and ^{72}As. *Nuclear Physics A*, vol. 121 (1968), 561–591. doi:10.1016/0375-9474(68)90109-7

[55] A. Rester, A. Ramayya, J. Hamilton, D. Krmpotic, P. Rao. Levels in ^{72}Ge populated by ^{72}Ga. *Nuclear Physics A*, vol. 162 (1971), 461–480. doi:10.1016/0375-9474(71)90248-X

[56] R. G. Helmer, C. van der Leun. Recommended standards for γ-ray energy calibration (1999). *Nuclear Instruments and Methods in Physics Research Section A: Accelerators, Spectrometers, Detectors and Associated Equipment*, vol. 450 (2000), 35–70. doi:10.1016/S0168-9002(00)00252-7

[57] N. Hayashi, H. Miyahara, K. Hara, *et al.* Highly accurate determination of γ-ray emission probabilities for ^{27}Mg. *Nuclear Instruments and Methods in Physics Research Section A: Accelerators, Spectrometers, Detectors and Associated Equipment*, vol. 422 (1999), 493–497. doi:10.1016/S0168-9002(98)01072-9

[58] R. Bigoni, S. Bloom, K. Tirsell. Beta-gamma (CP) correlation and gamma spectroscopy in ^{27}Mg. *Nuclear Physics A*, vol. 134 (1969), 620–632. doi:10.1016/0375-9474(69)90025-6

[59] H. Miyahara, Y. Ogata, K. Fujiki, K. Katoh, N. Marnada. Highly precise measurements of the relative gamma-ray intensities for ^{56}Mn and ^{72}Ga. *Applied Radiation and Isotopes*, vol. 60 (2004), 295–299. doi:10.1016/j.apradiso.2003.11.031

[60] K. G. Tirsell, L. G. Multhauf, S. Raman. Decays of ^{58}Mn, ^{57}Mn, and ^{56}Mn. *Physical Review C*, vol. 10 (1974), 785–794. doi:10.1103/PhysRevC.10.785

[61] J. Lachkar, J. Sigaud, Y. Patin, G. Haouat. Étude des niveaux de ^{56}Fe excités par les réactions (p, p'γ) ET (n, n'γ). *Nuclear Physics A*, vol. 222 (1974), 333–364. doi:10.1016/0375-9474(74)90395-9

[62] S. Raman, N. B. Gove, J. K. Dickens, T. A. Walkiewicz. Log ft values for second-forbidden β-transitions and the decay of ^{24}Na. *Physics Letters B*, vol. 40 (1972), 89–91. doi:10.1016/0370-2693(72)90291-2

[63] C. van der Leun, C. Alderliesten. The deuteron binding energy. *Nuclear Physics A*, vol. 380 (1982), 261–269. doi:10.1016/0375-9474(82)90105-1

[64] M. A. Islam, T. J. Kennett, S. A. Kerr, W. V. Prestwich. A self-consistent set of neutron separation energies. *Canadian Journal of Physics*, vol. 58 (1980), 168–173. doi:10.1139/p80-028

[65] T. Kishikawa, K. Nishimura, S. Noguchi. Gamma-Ray spectrometry with a Ge detector: an importance of instrument function on a new energy calibration method. *Nuclear Instruments and Methods in Physics Research Section A: Accelerators, Spectrometers, Detectors and Associated Equipment*, vol. 353 (1994), 285–290. doi:10.1016/0168-9002(94)91658-6

[66] G. Audi, A. Wapstra. The 1995 update to the atomic mass evaluation. *Nuclear Physics A*, vol. 595 (1995), 409–480. doi:10.1016/0375-9474(95)00445-9

[67] D. R. Tilley, H. R. Weller, C. M. Cheves. Energy levels of light nuclei A = 16–17. *Nuclear Physics A*, vol. 564 (1993), 1–183. doi:10.1016/0375-9474(93)90073-7

[68] A. G. Kozorezov, J. K. Wigmore, A. Owens, *et al.* Resolution degradation of semiconductor detectors due to carrier trapping. *Nuclear Instruments and Methods in Physics Research Section A: Accelerators, Spectrometers, Detectors and Associated Equipment*, vol. 546 (2005), 209–212. doi:10.1016/j.nima.2005.03.026

[69] J. Roth, J. H. Primbsch, R. P. Lin. Segmentation and Pulse Shape Discrimination Techniques for Rejecting Background in Germanium Detectors. *IEEE Transactions on Nuclear Science*, vol. 31 (1984), 367–371. doi:10.1109/TNS.1984.4333279

[70] D. R. Tilley, C. M. Cheves, J. L. Godwin, *et al.* Energy levels of light nuclei A=5, 6, 7. *Nuclear Physics A*, vol. 708 (2002), 3–163. doi:10.1016/S0375-9474(02)00597-3

Appendices

List of Identified Peaks from Background γ-ray Spectrum

Table A.1: Identified gamma-rays from the background γ-ray spectrum using the NuDat 3.0 database [12]. The columns are: the γ-ray energy from the NuDat 3.0 database; the radioisotope emitting the γ-ray; the relative intensity of the γ-ray; the peak position in the spectrum; and additional notes of the peak. Values from the NuDat 3.0 database (i.e. first and third column) are listed with numerical uncertainty in the nuclear data sheets style.

E_γ (keV)	Isotope	Rel. intensity (%)	E_{spec} (keV)	Notes
235.96 (2)	Th-227	12.9 (11)	235-243	U-235 decay chain
238.632 (2)	Pb-212	43.6 (5)		Th232 decay chain
240.986 (6)	Ra-224	4.10 (5)		Th232 decay chain
241.995 (4)	Pb-214	7.26 (4)		U-238 decay chain
269.463 (10)	Ra-223	13.30 (9)	269.77	U-235 decay chain
270.245 (2)	Ac-228	3.46 (6)		U-235 decay chain
271.23 (1)	Rn-219	10.8 (6)		U-235 decay chain
295.224 (2)	Pb-214	18.47 (11)	293.5-295.9	U-238 decay chain
293.5 (1)	Bi-215	14.7 (6)		U-235 decay chain
293.5 (1)	Bi-215	49 (6)		U-235 decay chain
299.98 (3)	Th-227	2.21 (20)	299.1	U-235 decay chain
300.066 (10)	Pa-231	2.41%(5)		U-235 decay chain
300.087 (10)	Pb-212	3.30 (4)		Th232 decay chain
328.000 (6)	Ac-228	2.95 (12)	327.3	Th232 decay chain
338.282 (10)	Ra-223	2.601 (18)	338	U-235 decay chain
338.320 (3)	Ac-228	11.27 (19)		Th232 decay chain
351.07 (5)	Bi-211	13.02 (12)	351.3	U-235 decay chain
351.9320 (21)	Pb-214	35.72 (24)		U-238 decay chain
409.462 (6)	Ac-228	1.92 (4)	408.7	U-238 decay chain
463.004 (6)	Ac-228	4.40 (7)	462.1	U-238 decay chain
510.77 (10)	Tl-208	22.60 (20)	510.2	U-238 decay chain
569.698 (2)	Pb-207	97.9 (14)	568.8	U-235 decay chain
583.187 (2)	Tl-208	85.0 (3)	582.2	U-238 decay chain
609.321 (7)	Bi-214	45.44	609	U-238 decay chain
661.657 (3)	Cs-137	85.10 (20)	661.2	Cs-137 natural decay
727.330 (9)	Bi-212	6.67 (9)	726.3	U-238 decay chain
768.360 (7)	Bi-214	4.889 (25)	767.6	U-238 decay chain
772.291 (5)	Ac-228	1.49 (3)	771.6	U-238 decay chain
785.37 (8)	Bi-212	1.102 (13)	785.2	U-238 decay chain
785.96 (9)	214PB	1.06 (8)		U-238 decay chain

E_γ (keV)	Isotope	Rel. intensity (%)	E_{spec} (keV)	Notes
794.947 (5)	Ac-228	4.25 (7)	794.7	U-238 decay chain
803.06 (3)	Pb-206	98 (7)	805.3	U-238 decay chain
806.179 (10)	Bi-214	1.262 (8)		U-238 decay chain
835.710 (6)	Ac-228	1.61 (6)	834.8	U-238 decay chain
860.557 (4)	Tl-208	12.50 (10)	860.4	U-238 decay chain
911.204 (4)	Ac-228	25.8 (4)	911	U-238 decay chain
934.056 (8)	Bi-214	3.094 (19)	933.6	U-238 decay chain
964.766 (10)	Ac-228	4.99 (9)	964.3	U-238 decay chain
968.971 (17)	Ac-228	15.8 (3)	968.1	U-238 decay chain
1063.656 (3)	Pb-207	88.8 (13)	1063.2	U-235 decay chain
1120.294 (6)	Bi-214	14.90 (8)	1119.2	U-238 decay chain
1155.210 (8)	Bi-214	1.634 (10)	1154.4	U-238 decay chain
1238.122 (10)	Bi-214	5.83 (3)	1236.6	U-238 decay chain
1280.976 (12)	Bi-214	1.435 (9)	1280.5	U-238 decay chain
1368.626 (5)	Na-24	99.9936 (15)	1367.6	Radioactive cosmogenic isotope
1377.669 (12)	Bi-214	3.985 (22)	1376.9	U-238 decay chain
			1383.7	Unidentified
1401.515 (13)	Bi-214	1.333 (8)	1401	U-238 decay chain
1407.988 (12)	Bi-214	2.388 (13)	1406.5	U-238 decay chain
1460.82 (5)	K-40	10.66 (17)	1460	K-40 natural decay
1509.211 (10)	Bi-214	2.127 (16)	1507.7	U-238 decay chain
1588.20 (3)	Ac-228	3.22 (8)	1587	U-238 decay chain
			1591.9	Tl-208 (se)
1620.50 (10)	Bi-212	1.47 (3)	1619.7	U-238 decay chain
1630.627 (10)	Ac-228	1.51 (4)	1629.3	U-238 decay chain
1661.274 (17)	Bi-214	1.046 (8)	1660.1	U-238 decay chain
1729.595 (15)	Bi-214	2.87 (3)	1728.1	U-238 decay chain
1764.491 (14)	Bi-214	15.29 (8)	1764	U-238 decay chain
1847.433 (17)	Bi-214	2.027 (16)	1847	U-238 decay chain
			2102	Tl-208 (fe)
2118.513 (25)	Bi-214	1.156 (10)	2116.8	U-238 decay chain
2204.10 (4)	Bi-214	4.92 (3)	2203.4	U-238 decay chain
			2222.1	Unidentified
2447.69 (3)	Bi-214	1.545 (11)	2446.5	U-238 decay chain
2610 (20)	Po-212	2.6 (3)	2613.3	U-238 decay chain
2614.511 (10)	Tl-208	99.754 (4)		U-238 decay chain
2754.007 (11)	Na-24	99.855 (5)	2753	Radioactive cosmogenic isotope

List of Identified Peaks from Background-Corrected γ-ray Spectrum

Table B.1: Identified gamma-rays from background-corrected γ-ray spectrum using the PGAA database [46], with the exception of the fast-neutron reaction of ^{16}O and ^{5}He. The columns are: the γ-ray energy from the PGAA database E_γ; the parent isotope of the thermal-neutron capture reaction; the cross-section of the thermal-neutron capture reaction from the PGAA database; the peak position in the spectrum E_{spec}; and additional notes of the peak. Most of the values from the PGAA database (i.e. first and third column) are listed with numerical uncertainty in the nuclear data sheets style.

E_γ (keV)	Parent Isotope	Cross-section (b)	E_{spec} (keV)	Notes
244.5420(20)	Cs-133	0.016(4)	243	
277.161(17)	Co-59	6.77(8)	277.9	
277.6310(20)	Cs-133	0.066(5)		
284.987(3)	Cs-133	0.044(5)	284.5	
296.165(4)	Cs-133	0.0084(22)	295.9-298.44	
297.41(3)	Ge-72	0.0414(12)		
297.99(5)	Co-59	0.0463(14)		
317.07(8)	Ge-74	0.0045(5)	318.5-321.1	
317.0720(20)	Cs-133	0.149(10)		
318.80(4)	Cu-63	0.0120(4)		
321.10(6)	Cu-63	0.0085(3)		
325.74(3)	Ge-72	0.0649(18)	323.82-326.54	
333.89(12)	Cu-65	0.0009(3)	333.2	
347.148(7)	Cs-133	0.073(6)	346.5-346.17	
347.152(4)	Cs-133	0.030(4)		
349.340(19)	K-39	0.00104(18)		
364.176(4)	Cs-133	0.008(5)	364.7	
384.290(5)	Cs-133	0.034(7)	384.6	
384.45(5)	Cu-63	0.0700(14)		
391.218(15)	Co-59	1.080(14)	391	
410.386(3)	Cs-133	0.005(5)	409.2-417.4	
410.928(12)	Ge-73	0.0025(6)		
411.57(21)	Fe-54	0.022(5)		
412.448(5)	Cs-133	0.051(13)		

E_γ (keV)	Parent Isotope	Cross-section (b)	E_{spec} (keV)	Notes
417.277(4)	Cs-133	0.095(17)		
431.580(15)	K-41	0.00245(18)	431.4	
438.9920(20)	Cs-133	0.140(9)	438	
472.09(4)	Ge-73	0.0015(15)	469.4-484.2	
476.75(3)	Ge-73	0.0016(14)		
477.13(16)	Si-28	0.00034(15)		
477.595(3)	B-10	716(25)		
479.080(4)	Cs-133	0.0038(16)		
479.624(6)	Cs-133	0.030(10)		
479.76(3)	Ge-73	0.0020(6)		
479.79(3)	Ge-73	0.0033(15)		
481.41(15)	Cu-65	0.0026(4)		
481.69(3)	Ge-73	0.0090(7)		
483.351(20)	Ni-62	0.0156(3)		
484.257(16)	Co-59	0.804(11)		
499.87(3)	Ge-70	0.162(6)	499.7	
510.795(3)	Cs-133	1.54(3)	510.1	511 keV gamma annihilation
532.17(7)	Co-59	0.0655(24)	532.6	
537.58(14)	Cu-65	0.00063(8)	537.9	
566.905(4)	Cs-133	0.006(5)	566.9-570.9	
567.32(7)	Cu-65	0.00107(12)		
567.483(4)	Cs-133	0.052(9)		
567.95(3)	Ge-73	0.0004(4)		
569.441(18)	K-41	0.00056(14)		
569.7	Pb-206	0.0014(3)		
569.7020(20)	Pb-206	1.06E-04(6)		
569.76(11)	Ge-74	0.0052(8)		
569.885(19)	Fe-56	0.0139(3)		
570.581(23)	Ge-73	0.0005(4)		
570.825(3)	Cs-133	0.221(12)		
570.90(3)	Fe-58	1.80E-04		
582.54(3)	Ge-76	9.30E-05(19)	582	
582.96(12)	Cu-63	0.0050(4)		
583.561(16)	F-19	0.00356(12)		
595.851(5)	Ge-73	1.100(24)	595.6	
608.353(4)	Ge-73	0.250(6)	607.5-609.5	
608.28(12)	N-14	2.5E-05(10)		
608.353(4)	Ge-73	0.250(6)		
608.766(23)	Cu-63	0.270(6)		
609.50(10)	Ni-64	2.20E-05(7)		
617.15(5)	Co-59	0.0570(22)	617	
628.85(10)	Ni-64	0.0013(3)	628.9	
632.68(9)	Cu-65	0.00083(24)	632.8	

E_γ (keV)	Parent Isotope	Cross-section (b)	E_{spec} (keV)	Notes
643.505(21)	Ge-73	0.0014(3)	644	
657.86(4)	Ge-73	0.0010(6)	657.3	
662.69(4)	Cu-63	0.072(3)	662.8	
670.656(21)	Ge-73	0.0043(6)	667.1-671	
667.821(19)	Ge-73	0.0040(6)		
670.57(9)	F-19	3.0E-06(10)		
670.656(21)	Ge-73	0.0043(6)		
671.148(22)	K-41	0.00028(9)		
685.37(20)	Ge-76	8.0E-06(8)	684.5-687.1	
685.37(20)	Ge-76	3.0E-06(3)		
685.647(25)	Ge-73	0.00097(25)		
686.940(13)	Ge-73	0.0006(3)		
691.960(19)	Fe-56	0.1370(18)	691.6-708.6	
692.0(8)	K-41	3.6E-06(8)		
692.16(4)	S-34	1.58E-05(21)		
692.23(14)	Ni-64	0.00029(8)		
692.43(5)	Ge-73	0.0006(4)		
692.670(3)	Cs-133	0.037(6)		
695.168(11)	K-41	0.00111(20)		
695.340(6)	Cs-133	0.039(10)		
695.67(15)	Cu-63	0.0021(3)		
695.688(15)	Ge-73	0.0033(6)		
697.44(17)	Fe-58	1.60E-05		
698.54(5)	Ge-76	2.72E-05(6)		
701.25(5)	Ni-60	1.7E-04(4)		
701.38(21)	Cs-133	0.036(10)		
701.509(8)	Ge-73	0.0642(19)		
702.7(3)	Ni-61	3E-05(6)		
702.75(12)	Fe-56	0.0013(7)		
703.290(5)	Cs-133	0.043(10)		
705.24(8)	Ge-76	1.27E-05(3)		
706.371(20)	Fe-56	0.0056(3)		
706.79(3)	K-41	6E-05(5)		
707.15(5)	S-32	1.0E-04(3)		
708.15(3)	Ge-70	0.0825(24)		
708.417(5)	Cs-133	0.220(11)		
708.646(4)	Cs-133	0.105(14)		
726.511(9)	Cs-133	0.013(13)	726.5	
728.76(3)	Co-59	0.024(6)	729.3	
735.102(9)	K-41	0.0027(3)	735.9	
739.769(4)	Cs-133	0.008(6)	739.9	
746.393(23)	Ge-73	0.0021(5)	746.5	
749.09(3)	Cr-50	0.569(9)	749.1	
754.43(13)	P-31	0.00028(3)	754.5	
765.962(23)	K-41	5E-05(4)	765	

E_γ (keV)	Parent Isotope	Cross-section (b)	E_{spec} (keV)	Notes
770.211(8)	Ge-73	0.0135(8)	769.9	
770.3050(20)	K-39	0.903(12)		
770.544(5)	Cs-133	0.104(11)		
779.59(4)	Cu-63	0.00382(20)	778.6	
784.91(10)	Ge-72	0.0049(6)	784.7-788.4	
785.628(21)	Co-59	2.41(7)		
786.73(3)	Ge-73	0.0009(5)		
787.2(6)	N-15	2.60E-15(5)		
788.38(14)	Cu-65	0.0009(4)		
802.84(23)	Ge-76	3.34E-06(13)	802.6	
810.70(6)	Cu-65	0.0026(4)	810.5	
822.673(24)	Cu-65	0.0238(17)	822.6	
823.95(9)	Ge-70	0.0029(6)	825.6	
834.2(3)	Cr-50	0.0022(6)	832.7-835.7	
834.849(22)	Cr-53	1.38(3)		
834.94(8)	Fe-56	0.0056(6)		
843.468(10)	K-39	0.0197(5)	843.1-847.2	
843.62(9)	Ni-58	0.00050(20)		
844.47(4)	Ge-73	0.0034(12)		
845.3(5)	Cr-50	0.0015(3)		
845.67(14)	Cr-53	0.0015(3)		
845.733(18)	Ni-62	0.0184(3)		
846.31(4)	S-33	2.2E-06(14)		
846.69(3)	K-41	8.9E-05(24)		
846.87(6)	Cu-63	0.0044(3)		
860.216(4)	Cs-133	0.014(7)	860.2	
867.4(4)	Fe-57	0.007(8)	866.6	
867.899(5)	Ge-73	0.553(12)		
874.093(13)	K-41	0.00049(14)	872.8-875.3	
880.343(4)	Cs-133	0.114(14)	879.4-882	
880.7(6)	Cr-54	6.8E-05(13)		
881.327(15)	Cs-133	0.022(8)		
881.47(3)	K-41	3.5E-05(11)		
897.07(17)	Cu-63	0.0102(4)	896.6-899.4	
897.90(14)	Pb-206	9.9E-05(9)		
898.27(3)	Fe-56	0.0540(10)		
898.98(3)	Si-30	2.3E-06(7)		
911.784(7)	Cs-133	0.177(14)	911	
916.29(15)	Ge-70	0.010(5)	917.3	
924.89(7)	Cu-63	0.00610(22)	924.1	
930.612(23)	Co-59	0.408(22)	930.8	
935.30(13)	Ge-70	0.0087(20)	934.6	

E_γ (keV)	Parent Isotope	Cross-section (b)	E_{spec} (keV)	Notes
942.67(4)	Si-30	1.3E-06(3)	942.8	
953.84(11)	Cu-63	0.0044(3)	952.7-956.8	
954.5(3)	Ni-64	5.100E-07(6)		
954.966(21)	Ge-73	0.0072(8)		
956.65(6)	Cu-65	0.0031(5)		
961.055(7)	Ge-73	0.129(4)	961.5	
978.28(3)	Ge-73	0.0016(10)	978.7	
982.951(10)	Al-27	0.00902(14)	984.4	
990.3(3)	Ge-76	2.8E-06(3)	990.9	
999.775(8)	Ge-73	0.0581(19)	999.1	
1005.668(22)	Co-59	0.127(6)	1005.4	
1013.588(10)	Al-27	0.00555(10)	1013.7	
1018.93(3)	Fe-56	0.0507(11)	1018.3	
1024.995(17)	N-14	1.26E-05(24)	1024.4	
1026.84(3)	K-39	0.00103(25)	1026.9	
1038.97(3)	Cu-65	0.0598(13)	1037-1039.5	
1049.51(4)	Ge-73	0.0032(17)	1047.9-1053	
1049.62(4)	Ge-73	0.0025(9)		
1049.63(3)	Ge-73	0.0032(9)		
1050.4(3)	Pb-204	1.0E-04(5)		
1051.97(7)	Ge-73	0.0012(9)		
1052.01(5)	Cu-65	0.0117(8)		
1052.54(15)	Ge-76	3.72E-06(13)		
1052.86(3)	K-41	1.5E-04(15)		
1063.662(4)	Pb-206	0.0013(3)	1063.1	
1075.66(10)	Co-59	0.099(7)	1075	
1081.72(3)	Cu-63	0.0117(3)	1081.8	
1084.68(3)	K-41	3.6E-05(11)	1084.3	
1088.61(13)	Cu-65	0.00084(8)	1089.7	
1095.42(5)	Ge-70	0.053(5)	1095	
1098.62(5)	Ge-70	0.0165(10)	1098.9	
1113.072(25)	K-39	0.00112(25)	1113-1117.1	
1113.34(3)	S-33	3.2E-06(5)		
1113.465(18)	Ni-58	0.00154(16)		
1114.56(4)	Ni-58	0.00142(15)		
1114.65(21)	Cs-133	0.049(10)		
1114.80(5)	Ge-76	1.23E-05(5)		
1115.53(4)	Ni-64	0.002190(13)		
1115.56(11)	Fe-56	0.0024(4)		
1115.76(24)	Cu-65	0.00058(11)		
1125.289(14)	Al-27	0.00083(4)	1125.7	
1128.72(7)	Ni-61	0.00123(15)	1129.8	
1133.84(7)	Ni-60	2.0E-04(4)	1133.8	

E_γ (keV)	Parent Isotope	Cross-section (b)	E_{spec} (keV)	Notes
1139.27(6)	Ge-70	0.0441(23)	1139.2	
1155.95(4)	K-41	6.2E-05(18)	1156.5	
1161.61(6)	Cu-65	0.00066(12)	1161.3-1165	
1162.11(3)	Fe-58	1.80E-05		
1162.50(4)	K-39	0.0065(11)		
1163.34(12)	Ni-61	0.00145(20)		
1164.65(12)	Ge-76	5.97E-06(13)		
1164.82(12)	Cr-50	0.00162(21)		
1172.84(5)	Ni-61	0.0122(4)	1172.5	
1178.396(21)	K-39	0.0069(8)	1177.9	
1188.781(13)	Ni-58	0.0559(9)	1189.9	
1189.69(6)	Ge-73	0.0087(9)		
1198.63(16)	Cu-63	0.00249(21)	1198.6-1202.6	H-1 se-peak
1200.75(10)	Ge-73	0.013(15)		
1200.89(18)	Ge-73	0.013(14)		
1200.94(3)	Ge-73	0.013(14)		
1201.272(7)		1.5E-04(5)		
1201.43(10)	Ge-76	9.69E-06(19)		
1208.59(16)	Cu-65	0.00030(18)	1208.5	
1212.53(4)	Cu-65	0.0105(5)	1212.6	
1226.118(17)	Ni-58	0.0126(4)	1226	
1236	O-18	5.6E-11(8)	1236-1238.6	
1236.057(24)	Ge-73	0.010(6)		
1236.506(23)	Ni-62	0.00195(17)		
1237.61(5)	S-33	4.0E-06(6)		
1237.81(11)	Fe-57	0.0035(3)		
1238.566(24)	Co-59	0.290(7)		
1244.39(7)	Ge-73	0.0075(9)	1245.2	
1244.64(3)	P-31	0.00357(17)		
1258.41(3)	Ge-73	0.010(5)	1259.3	
1260.448(19)	Fe-56	0.0684(11)		
1271.71(8)	Co-59	0.059(4)	1272.5	
1272.34(5)	Cu-65	0.0037(5)		
1273.349(17)	Si-28	0.0289(6)		
1298.10(3)	Cu-63	0.0147(7)	1298	
1302.62(6)	Ge-73	0.0022(13)	1302.3	
1302.64(23)	Cu-65	0.0029(5)		
1315(4)	Fe-54	0.0009(5)	1315.4	
1320.65(6)	K-39	0.0066(5)	1320.8	
1325.18(16)	S-33	2.6E-06(6)	1324.2-1327.9	
1326.05(8)	Ge-76	4.56E-06(13)		
1327.62(15)	Cu-63	0.00242(19)		
1332.82(19)	Pb-207	5E-06(3)	1332.8	

E_γ (keV)	Parent Isotope	Cross-section (b)	E_{spec} (keV)	Notes
1342.320(20)	Al-27	0.00209(6)	1342	
1345.77(6)	Cu-63	0.0155(3)	1345.5	
1349.02(17)	Fe-58	8.50E-06	1349.7	
1349.07(8)	Ge-70	0.0032(8)		
1364.86(10)	Al-27	0.00066(5)	1363.4	
1367.05(4)	Ge-73	0.0027(23)	1367.5	
1378.73(6)	Ge-70	0.017(4)	1377.5	
1381.43(4)	Ge-73	0.0014(7)	1381	
1384.158(13)	Ge-73	0.0099(8)	1385.1	
1390.95(3)	K-41	1.7E-04(4)	1390.2	
1395.276(17)	Ni-58	0.00500(22)	1396.8	
1399.069(20)	K-39	0.0104(5)	1399.1-1402.7	
1400.01(3)	K-41	0.00055(14)		
1401.29(15)	Cu-65	0.00044(9)		
1401.64(6)	Ni-60	7.0E-05(24)		
1401.67(23)	Cu-63	0.0029(3)		
1402.0(4)	Cr-54	1.38E-07(19)		
1407.894(11)	K-41	0.0025(5)	1407.6	
1411.8(5)	Ge-76	7.8E-07(21)	1411.5	
1431.72(7)	Ge-73	0.0029(22)	1431-1434.9	
1432.98(6)	P-31	2.2E-04(6)		
1433.245(12)	K-41	0.00066(20)		
1434.51(4)	K-39	0.0021(4)		
1439.37(5)	Cu-65	0.0111(16)	1441	
1446.176(22)	Si-28	0.00134(13)	1446.3	
1452.59(5)	Ge-76	1.44E-05(4)	1453.1	
1460.99(7)	Ge-73	0.004(4)	1461.1	
1480.024(24)	K-39	0.0353(9)	1481	
1481.68(9)	Cu-63	0.0025(3)		
1499.12(4)	Cu-63	0.0064(8)	1498.3	
1502.04(6)	Ni-60	0.0154(4)	1502-1508	
1502.08(19)	Cu-63	0.0031(7)		
1502.79(4)	K-39	0.0085(5)		
1502.87(7)	Ge-73	0.0019(7)		
1503.55(9)	Cr-53	0.0011(4)		
1505.14(17)	Co-59	0.062(16)		
1505.46(3)	Si-29	2.08E-04(11)		
1506.33(11)	Cu-65	0.00133(24)		
1506.74(15)	Fe-54	0.00133(22)		
1506.97(19)	Cr-53	0.0012(3)		
1507.33(3)	Co-59	0.463(9)		
1507.49(10)	Cr-53	0.0011(4)		
1515.720(25)	Co-59	1.740(25)	1516.5	
1521.03(4)	Cu-63	0.0143(5)	1521.7	
1528.20(5)	Ge-76	5.52E-06(13)	1529.1	

E_γ (keV)	Parent Isotope	Cross-section (b)	E_{spec} (keV)	Notes
1545.09(23)	Ge-74	0.007(3)	1545.1	
1552.62(13)	Cu-65	0.0027(3)	1553.1	
1558.08(6)	Cu-65	0.0025(10)	1558.5	
1567.96(7)	Ni-58	0.00042(9)	1567.6	
1571.84(3)	K-41	1.8E-04(5)	1571.8	
1575.45(3)	K-41	1.1E-04(5)	1575.7	
1578.84(4)	K-39	0.00073(8)	1579.8	
1582.50(4)	Cu-65	0.0094(7)	1581.8-1585.7	
1584.42(10)	Fe-56	0.0030(3)		
1585.12(3)	K-41	1.2E-04(3)		
1585.502(18)	S-33	1.95E-05(24)		
1592.124(21)	Ni-58	0.00130(14)	1591.8	
1598.48(4)	Ge-70	0.0044(6)	1599	
1604.36(4)	K-41	1.7E-04(6)	1603.8	
1611.11(18)	Co-59	0.028(5)	1611.9-1612.9	
1612.786(18)	Fe-56	0.1530(22)		
1615.16(16)	Pb-207	2.2E-05(3)	1616	
1622.877(18)	Al-27	0.00989(15)	1622.5	
1630.02(14)	Cu-63	0.0018(3)	1629.8	
1631.1(3)	Ge-70	0.0189(13)		
1635.84(7)	Ge-73	0.0138(11)	1635.8	
1642.42(3)	Al-27	0.00068(4)	1642.4	
1649.63(11)	Cu-63	0.0030(3)	1649.3	
1651.88(12)	Cu-65	0.00313(24)	1653.2	
1656.47(12)	Pb-204	8.8E-05(7)	1658.6	
1662.29(3)	Ni-60	0.00054(12)	1662.7	
1670.44(14)	Cu-65	0.00125(16)	1669.2	
1670.98(6)	Cu-63	0.0059(5)		
1675.73(4)	Ge-73	0.0080(8)	1675.9	
1679.642(20)	Ni-58	0.0039(3)	1680	
1681.24(5)	N-14	0.00129(8)	1682.7	
1687.17(7)	K-41	3.9E-05(11)	1688	
1693.1(10)	O-17	5.2E-08(10)	1693.1	
1697.24(3)	S-32	0.01250(25)	1697.3	
1710.877(24)	Fe-56	0.0038(4)	1710.7	H-1 fe-peak
1722.16(5)	Ge-76	6.10E-06(13)	1722.4-1726.1	
1722.38(10)	Fe-56	0.0074(6)		
1723.17(9)	Cu-65	0.0010(3)		
1724.92(6)	Ni-64	5.66E-05(18)		
1725.288(21)	Fe-56	0.181(3)		
1725.94(7)	K-39	0.00069(11)		
1770.39(3)	K-39	0.00065(19)	1769.9	
1775.82(3)	Ge-73	0.0033(13)	1775.7-1780.7	

E_γ (keV)	Parent Isotope	Cross-section (b)	E_{spec} (keV)	Notes
1778.92(3)	Al-27	0.232(4)		
1807.49(3)	Ge-73	0.0109(10)	1808.1	
1807.9(3)	Cr-50	0.0012(4)		
1858.48(3)	K-39	0.0108(5)	1860.2	
1861.848(10)	K-41	0.0028(4)		
1878.60(7)	Ge-76	4.36E-06(13)	1878.6	
1904.72(9)	Cu-63	0.0069(4)	1905.7	
1940.422(12)	Ge-73	0.0382(16)	1941.8	
1940.56(8)	Ge-70	0.0051(9)		
1941.05(3)	P-31	0.00413(20)		
1949.911(17)	Ni-58	0.0476(10)	1949.4	
1958.54(3)	Ge-73	0.0007(5)	1957.2-1959.5	
1959.69(3)	Ni-60	0.00050(12)		
1971.170(24)	Ge-73	0.0048(8)	1972.8	
1980.00(12)	Cu-65	0.00205(20)	1981.2	
1980.97(20)	Fe-56	0.0021(6)		
1981.95(9)	O-17	2.0E-07(4)		
2001.920(19)	N-14	1.9E-04(4)	2002.4	
2092.902(18)	Si-28	0.0331(6)	2092.6	
2104.26(24)	Fe-56	0.0030(3)	2103.4	
2112.00(7)	Ge-73	0.0020(10)	2111.3	
2223.25	H-1	0.3326(7)	2222.1	H-1 main peak
2300.34(4)	Ni-58	0.00071(12)	2300	
2301.44(5)	Ni-58	0.00071(12)		
2301.54(8)	Ni-61	0.0017(11)		
2614.18(3)	K-39	0.0165(6)	2613.6	
2614.53(3)	Pb-207	0.00040(3)		
2661.05(17)	Co-59	0.037(6)	2661.4	
2675.68(3)	Ge-73	0.0007(4)	2675.4	
2753.16(3)	S-32	0.0277(5)	2753.2	
2753.56(4)	Ge-73	0.0016(9)		
2753.66(4)	Ge-73	0.0049(22)		
2830.32(11)	Cu-63	0.0042(6)	2829.7	
2830.789(17)	N-14	0.00134(3)		
2861.4(3)	Co-59	0.040(8)	2861-2864.9	
2861.92(4)	K-41	2.2E-04(5)		
2862.010(12)	Al-27	7.4E-05(12)		
2862.04(3)	Ni-60	0.00168(17)		
2862.78(19)	Cu-65	0.0027(3)		
2863.01(7)	P-31	0.00359(18)		
2863.15(8)	Ge-73	0.0019(9)		
2864.516(25)	S-33	8.4E-05(11)		
2864.65(9)	F-19	2.2E-05(4)		
2973.42(4)	Al-27	4.7E-05(6)	2973.2	
2973.429(12)	Ge-73	0.0015(5)		

E_γ (keV)	Parent Isotope	Cross-section (b)	E_{spec} (keV)	Notes
2994.39(24)	Cu-63	0.0075(6)	2994.7	
2999.83(24)	Cu-63	0.0026(5)	2998.4-3009.4	
3004.90(4)	Ni-58	0.00325(16)		
3005.358(19)	S-33	7.7E-05(8)		
3007.0(4)	Co-59	0.058(6)		
3008.23(3)	K-41	1.26E-04(16)		
3009.06(13)	Cu-65	0.00179(16)		
3027.820(23)	K-39	0.0024(5)	3027	
3059.63(6)	Ge-73	0.0007(5)	3059-3062.4	
3060.81(5)	Fe-56	0.0034(4)		
3062.22(3)	Ni-60	0.00044(6)		
3168.40(10)	Fe-56	0.0092(7)	3168.2-3174.7	
3169.72(14)	Cu-65	0.00118(21)		
3172.60(22)	Cu-65	0.0045(3)		
3174.391(20)	S-33	8.1E-05(10)		
3337.75(7)	K-41	0.005(4)	3337.7-3343.3	
3338.05(6)	K-39	0.036(17)		
3338.50(5)	P-31	0.000367(20)		
3341.05(20)	Fe-58	3.90E-05		
3341.22(5)	Ge-73	0.0008(9)		
3343.04(3)	K-41	1.8E-05(17)		
3413.13(5)	Fe-56	0.0449(14)	3413.4	
3426.90(17)	Ge-73	0.0038(7)	3426.2-3440.3	
3428.1(3)	K-41	2.2E-04(4)		
3429.54(12)	Cu-65	0.0063(4)		
3429.98(6)	K-41	2.3E-04(5)		
3431.72(11)	Cu-63	0.0057(7)		
3434.39(6)	Ge-73	0.0005(4)		
3435.19(3)	Ge-73	0.0023(6)		
3436.66(9)	Fe-56	0.045(4)		
3538.43(9)	Ge-73	0.0018(10)	3536.7-3539.5	
3538.966(22)	Si-28	0.1190(20)		
3539.74(6)	K-41	3.2E-05(7)		
3683.920(9)	C-12	0.00122(3)	3681.3-3685.1	
3849.111(8)	Al-27	0.00699(17)	3849.1-3854.5	
3852.4(12)	Ge-72	0.0015(4)		
3853.60(6)	Ni-58	0.00129(6)		
3854.51(6)	Fe-56	0.0333(12)		
3911.43(5)	K-39	0.0168(9)	3911.7	

E_γ (keV)	Parent Isotope	Cross-section (b)	E_{spec} (keV)	Notes
3924.26(25)	Cu-65	2.2E-04(7)	3924.1-3956.9	
3926.48(5)	P-31	0.00368(14)		
3926.799(24)	Al-27	4.5E-05(6)		
3927.48(10)	Cr-53	0.0098(6)		
3929.84(12)	Co-59	0.272(11)		
3929.98(4)	Ni-58	0.0120(4)		
3930.52(5)	P-31	0.00108(5)		
3930.63(4)	K-39	0.0275(11)		
3934.59(6)	S-32	0.00035(6)		
3935.272(12)	Al-27	0.00063(5)		
3935.94(5)	K-41	1.6E-05(15)		
3937.44(4)	Ni-58	0.00030(3)		
3943.78(3)	K-39	0.0205(11)		
3946.21(7)	P-31	1.08E-04(6)		
3949.23(9)	S-33	1.19E-05(16)		
3950.00(4)	Ni-60	0.00136(12)		
3951.40(17)	Ni-64	2.3E-04(4)		
3952.21(4)	Ni-58	0.00095(8)		
3954.39(3)	Si-28	0.00449(19)		
3955.15(10)	Cu-65	0.00057(13)		
3955.32(19)	Ge-73	0.0018(4)		
3956.66(5)	Ni-60	3.5E-05(7)		
4013.71(4)	K-41	0.00068(13)	4012.8	
4218.27(5)	Fe-56	0.099(3)	4217	
4297.40(11)	Fe-57	0.0036(5)	4297.8	
4298.20(21)	Cu-65	0.00134(11)		
4404.44(4)	K-41	1.3E-04(12)	4404.4	
4404.69(4)	Ni-60	0.00388(25)		
4421.56(5)	Ni-58	6E-05(3)	4421.5	
4422.9(3)	Cu-63	0.0050(4)		
4430.60(4)	S-32	0.0262(6)	4430.7-4471	
4431.27(6)	K-39	0.0093(8)		
4433.38(11)	Cr-53	0.0036(7)		
4435.9(5)	Ge-74	0.0035(8)		
4436.69(14)	Cu-65	0.00032(11)		
4437.08(4)	Ge-73	0.0028(9)		
4441.1(3)	Cu-63	0.0070(10)		
4442.30(6)	K-41	7E-05(7)		
4443.04(4)	Ni-58	2.4E-04(3)		
4443.9(3)	Cu-63	0.0110(11)		
4443.99(7)	Ge-73	0.0010(5)		
4444.03(11)	B-10	0.039(3)		
4444.47(24)	Co-59	0.045(7)		
4445.11(14)	S-32	0.00065(11)		
4450.35(15)	Cu-63	0.0061(5)		

E_γ (keV)	Parent Isotope	Cross-section (b)	E_{spec} (keV)	Notes
4451.21(8)	Ge-73	0.0011(4)		
4451.37(11)	Cr-53	0.0078(8)		
4453.10(8)	Ni-58	2.1E-04(6)		
4455.1(17)	Fe-54	0.0019(10)		
4455.54(4)	P-31	0.000310(16)		
4456.03(5)	Ni-60	7.0E-05(8)		
4456.82(9)	K-41	1.1E-05(11)		
4457.52(20)	Cu-65	0.00132(14)		
4459.0(6)	Ni-62	2.1E-04(6)		
4459.21(19)	Cr-53	0.0068(11)		
4461.53(7)	Al-27	8.2E-05(6)		
4461.68(5)	Ni-58	6E-05(4)		
4462.67(3)	S-33	6.1E-05(8)		
4463.00(6)	Ge-73	0.0074(10)		
4463.01(10)	Fe-56	0.0162(11)		
4464.96(4)	K-41	8E-06(3)		
4468.54(11)	Cu-65	0.00162(16)		
4469.71(10)	Co-59	0.061(8)		
4690.676(5)	Al-27	0.01090(24)	4690.8	Al-27 se-peak
4893.76(10)	Co-59	0.217(11)	4896.7	Cs-133 se-peak
4933.889(24)	Si-28	0.1120(23)	4933.4	
4945.301(3)	C-12	0.00261(5)	4945	
4951.91(6)	Ge-73	0.0090(14)	4952.6	
4968.49(4)	Ni-60	2.28E-04(21)	4967.6	
4980.5(6)	Ge-70	0.0049(10)	4979.8	
4994.98(6)	Ge-73	0.0011(14)	4995	Fe-56 se-peak
4998.99(9)	Ge-73	0.0015(14)	4998.3	
5003.23(6)	Ge-74	0.0033(8)	5003.6	
5088.00(3)	Ge-73	0.0096(20)	5086.1-5090.5	
5088.13(6)	Ge-73	0.0029(5)		
5088.4(5)	Ge-74	0.0047(11)		Co-59 se-peak
5103.711(8)	Al-27	0.00097(6)	5099.7-5109.8	
				O-16 se-peak
5206.5(4)	Cr-50	0.0014(4)	5203	Al-27 fe-peak
5396.0(9)	Ge-72	0.0010(3)	5395.6	
5411.077(8)	Al-27	0.00481(19)	5408.8	Cs-133 fe-peak
5505.46(20)	Cs-133	0.333(22)	5505.9	Fe-56 fe-peak
			5598.5	Co-59 fe-peak
			5617.2	O-16 fe-peak
5709.853(13)	Al-27	0.00148(8)	5714.1	Al-27 peak
5914.935(17)	Cs-133	0.047(8)	5918.8	Cs-133 peak
6015.58(8)	Cu-63	0.0083(8)	6013.8-6022.1	Fe-56 peak
6018.532(20)	Fe-56	0.227(5)		
6089.997(17)	Cs-133	0.0015(5)	6092.1	

E_γ (keV)	Parent Isotope	Cross-section (b)	E_{spec} (keV)	Notes
6110.81(6)	Co-59	0.213(11)	6109.9	Co-59 peak
6128.63(4)	O-16		6128.7	O-16 peak (fast-n process)
			6190.6	Co-59 se-peak
6258.58(6)	Ni-58	0.0011(4)	6256	
6341.01(6)	Co-59	0.019(6)	6431.1	
6390.29(5)	Ge-72	0.0299(19)	6391.3	
6418.62(4)	Ge-72	0.0178(15)	6419.2	
6607.45(4)	Ge-70	0.00164(12)	6608.4	Ge-73 se-peak
			6621.6	Fe-56 se-peak
			6704	Co-59 fe-peak
6729.38(9)	Pb-204	0.00320(10)	6730.4	
			6767.4	S-32 se-peak
			6903.5	Cr-52 se-peak
7114.372(17)	Ge-73	0.0040(10)	7118.2	Ge-73 fe-peak
			7134.9	Fe-56 fe-peak
7214.42(3)	Co-59	1.38(3)	7211.8	Co-59 peak
			7279.1	S-32 fe-peak
7306.93(4)	Cu-63	0.321(17)	7307.2	
			7346.8	N-14 se-peak
7415.510(23)	Ge-70	0.016(5)	7413.8	Cr-52 fe-peak
7491.54(3)	Co-59	1.16(3)	7490.1	
			7555.6	Ni-58 se-peak
7526.014(18)	Ge-73	0.0020(15)	7631.4	Ge-73 peak
7626.309(16)	Ge-73	0.0034(4)		
7645.5450(10)	Fe-56	0.549(11)	7645.6	Fe-56
7724.027(4)	Al-27	0.0493(15)	7722.9	
7799.815(24)	S-32	0.0144(5)	7790.4	S-32 peak
7819.517(21)	Ni-60	0.336(6)	7819.8	
			7861.3	N-14 fe-peak
7915.62(4)	Cu-63	0.869(20)	7913.2	
7938.46(23)	Cr-52	0.424(11)	7938.9	Cr-52
			7974.9	Ni-58 se-peak
7997.66(3)	Ge-73	2.4E-04(22)	7997.9	
			8021.8	Ni-58 fe-peak
			8067.1	N-14 fe-peak
			8276.6	Fe-54 se-peak
8310.161(19)	N-14	0.00330(6)	8371.2	N-14 peak
8482.80(9)	Cr-50	0.169(7)	8486.2	Ni-58 fe-peak
8533.509(17)	Ni-58	0.721(13)	8535	Ni-58
8568.71(4)	N-14	5.4E-05(5)	8578.9	N-14 peak
			8696.1	Cr-53 se-peak
			8785.5	Fe-54 fe-peak
8884.36(5)	Cr-53	0.78(5)	8879.5-8890.2	
8886.18(23)	Fe-54	0.0162(12)		
8998.414(15)	Ni-58	1.49(3)	8999	Ni-58 peak

E_γ (keV)	Parent Isotope	Cross-section (b)	E_{spec} (keV)	Notes
9206.70(5)	S-33	2.7E-06(4)	9207.6	Cr-53 fe-peak
9297.68(19)	Fe-54	0.0747(25)	9298	Fe-54 peak
9719.06(5)	Cr-53	0.260(18)	9716.5	Cr-53 peak
			14834	Compton edge from 15.5 MeV
	He-5		15318	2nd exc. state to 1st exc. state
			16448	Compton edge from 16.7 MeV
	He-5		16680	2nd excited-state to g.s.

Table B.2: Identified gamma-rays from background-corrected γ-ray spectrum using ENSDF [47], and other relevant literature. The columns are: the fast-neutron reaction process; the γ-ray energy; and the intensity of the γ-ray, presented as relative (rel.) or absolute (abs.) values.

Reaction	E_γ (keV)	Intensity
^{74}Ge(n,n'γ)^{74}Ge	595.5	100% (rel.)
^{74}Ge(n,p)^{74}Ga$\xrightarrow{\beta^-}$ ^{74}Ge	595.87	92% (abs.)
^{74}Ge(n,n'γ)^{74}Ge	608.4	18.2% (rel.)
^{74}Ge(n,p)^{74}Ga $\xrightarrow{\beta^-}$ ^{74}Ge	608.4	15.7% (abs.)
^{72}Ge(n,n'γ)^{72}Ge	630	86% (rel.)
^{72}Ge(n,p)^{72}Ga $\xrightarrow{\beta^-}$ ^{72}Ge	630	26.16% (abs.)
^{208}Pb(n,n'γ)^{208}Pb	683.187	57% (rel.)
^{72}Ge(n,p)^{72}Ga$\xrightarrow{\beta^-}$^{72}Ge	834	95.5% (abs.)
^{27}Al(n,p)^{27}Mg $\xrightarrow{\beta^-}$ ^{27}Al	843.76	71.8% (abs.)
^{56}Fe(n,p)^{56}Mn $\xrightarrow{\beta^-}$ ^{56}Fe	846.76	98.85% (abs.)
^{56}Fe(n,n'γ)^{56}Fe	846.8	100% (not specified)
^{27}Al(n,p)^{27}Mg $\xrightarrow{\beta^-}$ ^{27}Al	1014.52	28.23% (abs.)
^{56}Fe(n,n'γ)^{56}Fe	1238.3	100% (not specified)
^{27}Al(n,α)^{24}Na $\xrightarrow{\beta^-}$ ^{24}Mg	1368	99.9936% (abs.)
^{208}Pb(n,n'γ)^{208}Pb	2614.511	100% (rel.)
^{27}Al(n,α)^{24}Na $\xrightarrow{\beta^-}$ ^{24}Mg	2754	99.855% (abs.)